Acoustic Pressure Mode Shapes and Frequencies in a Circular Tube for an Arbitrary Temperature Distribution

Cody M. Shelton* and Joseph Majdalani[†]

Auburn University, Auburn, AL 36849

In this work, an asymptotic expansion is presented that takes into account a naturally-occurring perturbation parameter in the context of a circular tube with an open-open endpoint configuration. This approach is shown to produce accurate predictions of pressure mode shapes and frequencies for arbitrary temperature distributions that mimic a wide variety of flow heating arrangements including, but not limited to, those associated with a Rijke tube. The underlying formulation consists of two linearly coupled partial differential equations that can be solved simultaneously while using a Green's function to capture the thermoacoustic pressure. In the present investigation, the strategy leading to an accurate prediction of the unsteady pressure oscillations is fully detailed and then applied to several representative cases. Results pertaining to the pressure oscillations are systematically discussed and compared to other recently developed models in the literature.

Nomenclature

a_0	mean speed of sound inside the Rijke tube
$A_{ m hs}$	surface area of obstacle or heater element
C_p	constant pressure specific heat
h	heat transfer coefficient
\overline{I}	acoustic intensity
k	thermal conductivity
L	internal tube length
m	longitudinal oscillation mode, $m = 1, 2, 3,$
p'	oscillatory pressure component
Q	heat
q	heat transfer rate, dQ/dt
q'	oscillatory heat transfer rate
T	temperature
t	time
u'	oscillatory velocity component
u_q	velocity fluctuations at the heater location
ϑ	volume
x	axial distance from the bottom-end
Greek	
γ	average ratio of specific heats

air density

complex frequency σ

mode shape

circular frequency, $m\pi a_0/L$

Subscripts

hs refers to the heat source

surrounding mean flow condition ∞ 0 denotes a steady or mean component

derivative with respect to the axial coordinate

^{*}Graduate Research Assistant, Department of Aerospace Engineering, Member AIAA.

[†]Professor and Francis Chair, Department of Aerospace Engineering, Assoc. Fellow AIAA.

I. Introduction

The fundamental mechanisms that affect the operation of a Rijke tube have often been the subjects of investigation and interpretation by several prominent researchers. One may cite the works of Carrier [1], Chu [2], Miller and Carvalho [3], Maling [4], Zinn [5], and the survey by Raun et al. [6]. The only aspect of the Rijke tube that is presently lacking full understanding is perhaps limited to the detailed interplay between the heat source, thermal patterns, and resulting acoustic motion. Functions have been proposed to relate interactions between the heat source and velocity perturbations, but these have not been completely effective at predicting the observed coupled interactions. In practice, complex interactions occur in two banded regions that are separated by a diffuse interface delineating a zonal discontinuity across the heat source. The resulting problem continues to draw attention, especially when the unsteady heat transfer in different segments of the tube is accounted for.

With these issues at hand, the present investigation is carried out in an attempt to further explain the unsteady heat transfer mechanisms that cause the heat-driven oscillations in a Rijke tube. It represents an extension to a previous study that devoted itself to the numerical simulation of the Rijke's internal flowfield [7]. We recall here that the phenomenon of heat-driven acoustic oscillations belongs to the field of thermoacoustics, a discipline that focuses on the interactions between heat and sound. In this context, whenever an unsteady heat source is introduced into a chamber, the potential for heat-driven acoustic oscillations exists. Typically, high intensity sound pressure levels are generated by the incumbent acoustic oscillations in systems exhibiting a likeness to Rijke [8] or Soundhauss [9] tubes. Consequences of such interactions may be either desirable or unfavorable depending on the type of application.

In practice, thermoacoustic systems have been devised to perform beneficial functions in a variety of industrial applications. Examples abound and one may include: promoting higher combustion efficiency [10–12], fuel savings [13, 14], controlled waste incineration [15], slurry atomization [16], reduced pollutant formation [17–26], increased fuel residence time in combustion chambers [27–29], increased convective heat transfer rates [30], and lower operating and equipment costs [13, 31, 32]. The basic mechanisms that trigger these beneficial outcomes are invariably associated with controlling the acoustic field [31] in such a way to improve mixing [33], heat transfer [14, 34–37], or both.

One of the archetypal applications of thermoacoustics arises in the context of coal-fired furnace [14, 20, 28, 31] and gas turbine operations [6, 35, 38]. In addition to its role at improving combustion efficiency, a pulsating pressure field can be effectively used to increase the size of exhaust particles. In the absence of user intervention, these particles can escape along with the flue gases to the extent of contributing to air pollution. In fact, conventional removal methods allow over 70% of the particles in the form of fine particulates to escape. Practically, however, particles smaller than about 5 microns are not efficiently removed. As a remedy, it has been demonstrated that the control of thermoacoustic energy can be effective at promoting the agglomeration of fine ash particles that are entrained in high temperature gas streams [17–21, 39].

As the name suggests, acoustic agglomeration is a process by which high intensity sound can be used to assemble micron and submicron sized particles in aerosols. The effect of sound is to cause relative motions between particles to the extent of increasing their collision rates. As particles collide, they tend to bond and form larger particles. As a result, the average particle size in the aerosols can be made to increase over a short period of time. Naturally, the larger particles can be more effectively separated from exhaust gases by conventional particulate removal instruments. This thermoacoustic process holds the benefit of reducing particulate emissions and simplifying clean-up systems. In addition to agglomeration control, acoustic energy can be employed to increase the rate and extent of coal combustion, thus allowing combustors to release larger amounts of heat [14, 35–37].

Contrary to their function in industrial applications, heat-driven oscillations in ramjet engines [40] and solid propellant rocket motors [41] are viewed as being undesirable. Corresponding thermoacoustic noise has often been referred to as chugging, buzzing, screening, screeching, or squealing, depending on its frequency range and severity. These audible oscillations can, at times, cause unwanted vibrations to plague instrumentation and payloads to the point of modifying rocket performance and throwing a missile off course [42].

Due to the commonality of features shared rather ubiquitously by pulse combustion devices, the coupling aspects in a Rijke tube may be manifested in a variety of problems incorporating heat, pressure, and velocity perturbations. Over time, detailed investigations of thermoacoustics and combustion stability prediction methods for Rijke tubes have helped to advance our understanding of these problems. These have encompassed both linear and nonlinear stability schemes that are capable of predicting characteristic stability features such as critical frequencies, amplitudes, growth rates, limit-cycle oscillations, and the intricate relations between pressure, velocity, and heat release [43–46]. On this count, one of the first prominent analytical models of Rijke tubes may be attributed to Nicoli and Pelce [47]; their asymptotic analysis has since been shown to effectively predict the Rijke's flame transfer function. Along similar lines,

Hantschk and Vortmeyer [48] have shown that favorable agreement between their control-volume computations and experiments could be achieved by introducing nonlinearities in limit-cycle amplitudes triggered by the heat release feedback from the Rijke's heating element. Matveev and Culick [49–51] have also developed a very elegant model to predict the stability boundaries of a Rijke tube as a function of several salient parameters, such as the power supplied or the mass flow rate.

Among his conclusions, Matveev [51] pinpoints the importance of accurately representing the axial temperature gradient along the tube to avoid underpredicting the stability margins with a simplistically uniform mean temperature. Unless thermal nonlinearities are accounted for, it is shown that the Rijke's hysteresis behavior in the stability boundary at a high mass flow rate cannot be adequately predicted by an otherwise linear thermal model. His work establishes the criticality of quantifying the thermal profile as well as the nonlinearity in the transfer functions being implemented between the heat release and one or more of the other acoustic variables.

A decade later, Bigongiari and Heckl [52, 53] use a Green's function approach to model the Rijke tube's internal flowfield, particularly, the heater-induced velocity; their work leads to robust predictions that are comparable in accuracy to those obtained from a computationally-based control volume approach. In fact, when compared to other available techniques, the Green's function approach is proven to be advantageous in its rapid implementation and prediction of local properties around obstacles and segmented zones along the length of tube [54, 55]. Moreover, the Green's function approach enables the user to incorporate a rather simple nonlinear heat release correlation in conjunction with a non-uniform axial temperature distribution. Accordingly, the tube can be partitioned into segments that help to alleviate some of the issues encountered in other simulation methods.

Around the same timeframe, Juniper [56] undertakes an investigation of the triggering mechanism in a Rijke tube using an adjoint-based method. The latter is shown to be effective at identifying the most critical initial states as well as predicting the limit-cycle amplitudes using a numerical solution of the nonlinear governing equations. Also using an adjoint-based approach, Magri and Juniper [57] are able to define the feedback mechanisms that can be effective at suppressing thermaoustic instabilities that emerge in an oscillatory, heat-driven system. Among their findings, they show that the most critical state can be directly related to a heat release parameter, and that even a small perturbation of energy in the linear stable region can be sufficient to trigger high-amplitude oscillations. Subsequently, Juniper and Sujith [58] address the sensitivity of thermoacoustic oscillations in the linear regime, specifically exploring the impact of the heat release time lag and the phase relation between pressure and heat oscillations. They determine that both of these quantities can have overall destabilizing effects on the system. Along similar lines, Balasubramanian and Sujith [59] employ a numerical Galerkin appoach to demonstrate that the non-normal nature of thermoacoustic systems is sufficient to promote transient growth in an otherwise linearly stable system.

As for Zhao and Chow [60], they carry out a Rijke tube investigation that is focused on the adaptation of a hydrodynamic flame region around the heater, thereby simulating a laminar premixed flame from a Bunsen burner that can be thoroughly tested experimentally. They report that the location of the hydrodynamic zone can play a key role in the system's stability and nonlinear characteristics due, in large part, to the frequency's dependence on the location of applied heat. Their findings support Matveev's earlier conclusion that the temperature gradient within the tube plays an appreciable role in controlling instabilities. They also suggest that, since the interactions between acoustic disturbances and heat release are fundamentally non-normal, they can be either "constructive or destructive." In this vein, placing the heater around the well-known quarter-length location may be viewed as being the most destructive stability-wise. At the outset, any supplemental energy will tend to amplify the growth of unstable modes, while possibly triggering non-linear, limit-cycle behavior. Naturally, losses due to viscous damping, heat transfer, or the presence of a hydrodynamic region can slightly alter the critical quarter-length location [48, 52, 53, 56, 60].

In the present investigation, a brief description of pulse combustors will be given at first in Sec. II. This will be followed by a review of the fundamental concepts used to relate thermal fluctuations to acoustic pressure and velocity oscillations. In Sec. III, a standard similarity analysis will be used to identify the non-dimensional parameters that may be needed to establish a condition of similitude. In Sec. IV, the test apparatus used in the experimental investigation will be discussed and its results will be leveraged to validate other models and speculations. A computational model is also presented in Sec. V, followed by a discussion of independently obtained experimental and numerical data. In Sec. VI, the numerical simulations will be shown to be in favorable agreement with existing experimental and theoretical findings to the point of providing useful predictive tools. These observations will help to clarify existing speculations and support, in Sec. VII, two analytical formulations developed sequentially by Matveev and Heckl using either either a differential equation or Green's function techniques. In extending this line of inquiry, an asymptotic approximation of the heat-driven acoustic pressure and velocity equations will be introduced in Sec. VIII. More specifically, assuming a small nonlinearity in the heat release term, expressions will be derived to predict the onset of

acoustic pressure fluctuations in the presence of an arbitrary temperature gradient and a fluctuating heat source. The resulting perturbation expansion will be solved using the Green's function approach[52–55], thus leading to a relatively straightforward formulation. Then, using several thermal profiles in an open-open enclosure, the latter will be shown to predict the acoustic pressure mode shapes, peak pressure antinodes, and modal frequencies with a substantial degree of accuracy.

II. On the Rijke Tube and Pulse Combustion

Inasmuch as conventional combustion involves steady-state fuel consumption, pulse combustion differs at the fundamental level, especially in the presence of unsteady and often periodic phenomena that accompany the burning process [28]. The oscillatory behavior can occur spontaneously or it can be triggered by an external device, such as a spark plug, an igniter, or an acoustic driver. Pulsation becomes appreciable when the heat of combustion is released at one of the system's natural frequencies. Subsequent wave interactions with the combustion process result in sustained heat flux fluctuations. So far, studies of the underlying mechanisms have suggested that the strength of the thermoacoustic coupling remains contingent on the magnitude of the root mean square (RMS) of the heat input within the system. In order for the oscillations to persist, the rate at which heat is removed from the system must not exceed the rate at which acoustic heat energy is produced. Bearing these various perspectives in mind, a Rijke tube, which is classified as a pulse combustion device [61], is pictured schematically in Fig. 1.

A. Fundamental Wave Equations

The wave equations for a constant temperature duct with the heat addition term acting as a driving mechanism can be written for the acoustic pressure and velocity using [2]

$$\frac{1}{a_0^2} \frac{\partial^2 p'}{\partial t^2} - \nabla^2 p' = \frac{1}{C_p T_0} \frac{\partial q'_{\theta}}{\partial t} , \qquad (1)$$

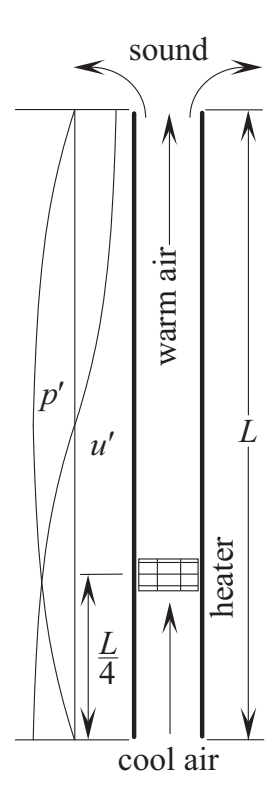


Fig. 1. Schematic of a Rijke tube of length L.

$$\frac{\partial^2 u'}{\partial t^2} - a_0^2 \nabla^2 u' = \frac{1 - \gamma}{\rho_0} \frac{\partial q'_{\theta}}{\partial x} , \qquad (2)$$

where p', u', and q'_{ϑ} denote the time-dependent pressure, velocity, and heat transfer rate per unit volume in onedimensional space; moreover, x, t, ρ_0 , T_0 , a_0 , C_p , and γ stand for the axial distance from the lower edge of the Rijke tube, time, average air density, average air temperature, constant pressure specific heat, and ratio of specific heats, respectively. Equations (1) and (2) can give rise to self-excited or "feedback" oscillations owing to the nature of the source terms. Since the unsteady heat release rate q' that appears in Eqs. (1) and (2) is not externally controlled, but rather induced by fluctuations in other properties within the system, the Rijke tube may be further classified as a self-excited oscillator.

Through inspection of Eqs. (1) and (2), three unknown variables may be readily identified. These are u', p', and q'. The dependence of q' on the acoustic pressure and velocity must therefore be established before closure to the problem can be achieved. Moreover, proper auxiliary conditions in the vicinity of the heat source must be expressed. Since no analytical formulation can be directly derived from Eqs. (1) and (2) without an additional equation that sets the model's character, an appropriate relation linking q' to p' or u' must precede further theoretical developments. In what follows, such a relation will be explored, specifically, after reviewing existing closure equations.

B. Pressure Coupling Relation

Chu [2] assumes that, in thermoacoustical systems, the rate of heat addition may be taken to be directly proportional to the rate of acoustic pressure. Accordingly, one may set

$$\frac{q'}{C_p T_0} = K p',\tag{3}$$

where K can be taken to be a constant. When inserted into Eq. (1), one obtains

$$\frac{1}{a_0^2} \frac{\partial^2 p'}{\partial t^2} - \nabla^2 p' = K \frac{\partial p'}{\partial t} . \tag{4}$$

Forthwith, the solution of Eq. (4) may be shown to be strictly decaying for $K \le 0$, and growing for K > 0. Additionally, Chu suggests letting $\bar{\varepsilon} \equiv K/(p_0^2 - p'^2)$ such that

$$\frac{1}{a_0^2} \frac{\partial^2 p'}{\partial t^2} - \nabla^2 p' = \varepsilon_0 \left(p_0^2 - p'^2 \right) \frac{\partial p'}{\partial t},\tag{5}$$

where p_0 refers to the average pressure. This last equation describes self-sustained, large-amplitude pressure disturbances that continue to increase until a steady limit-cycle oscillation state is reached. In actuality, Chu's pressure coupling concept proves effective at explaining how heat and pressure oscillations can be self-sustaining. However, it does not address why driving cannot occur at a velocity node despite the co-location of peak pressure amplitudes. Moreover, Eq. (5) is somewhat non-compliant with the Rayleigh criterion; the latter requires oscillatory amplitudes to increase when

$$\oint q'p' \, \mathrm{d}t > 0.$$
(6)

In Eq. (6), the symbol \oint is used to denote integration over one oscillation cycle. In short, although Chu's assumption remains valid for closed-open systems resembling the Soundhauss singing tube [9], it does not quite apply to Rijke tubes [8].

C. Velocity Coupling Relation

Instead of attributing the coupling of heat oscillations to internal pressure fluctuations, another proposed relation suggests that heat itself or velocity oscillations may stand behind the self-sustained motion. For example, Zinn [5] and Zinn et al. [62] assume that, for a combustion-driven Rijke tube, the heat transfer from the source to the gas can depend on the magnitude of the total instantaneous velocity. Mathematically, this hypothesis translates into

$$q = C_0 + C_1 |u_0 + u'| = C_0 + q_0 + q'. (7)$$

Here, C_0 and C_1 represent two pure constants, u_0 denotes the mean flow velocity, and u' alludes to the acoustic velocity. This relation may be viewed as an improvement over the foregoing formulation wherein acoustic excitation is attributed to pressure coupling alone.

D. Energy Coupling Relation

So far, we have reviewed two simple expressions by Chu [2] and Zinn [5] that relate heat oscillations to either the pressure or the velocity coupling mechanisms via Eqs. (4) and (7). Our forthcoming analysis, however, leads us to suspect a different functional form. Before delving into more detail, we bring the reader's attention to the prevalent symmetry in the coupled set of differential equations formed by Eqs. (1) and (2). This symmetry suggests that heat oscillations are more likely to be a function of both acoustic pressure and velocity, than a sole function of either of the two. At the outset, a possible relation between q' and the product of the two acoustic quantities, p' and u', may be considered. This hypothesis is further supported by work conducted on planar flames by McIntosh [63]; therein, the unsteady heat release is shown to be dependent on both the pressure and velocity fluctuations through the underpinning combustion dynamics. In this vein, a symmetric expression can be constructed by positing a relation between heat oscillations and the energy-flux vector modulus, ||p'u'||. This proposed form will be further discussed, refined, and justified below.

III. Scaling Analysis

A. Theoretical Considerations

It is well known that when heat is added to a volume of fluid, its density diminishes, thus leading to an expansion of the heated flow. The periodic expansions and contractions of this volume due to unsteady heat release triggers the formation of pressure waves in a Rijke tube. These pressure waves can, in turn, influence the time-dependent thermal oscillations around the heater. In fact, amplified heat oscillation amplitudes are often reported in a Rijke tube when the heat source is placed at a point where both acoustic pressure and velocity have nonzero amplitudes that are additive, i.e., when they overlap with a favorable phase. Experimental observations also corroborate that when the heat source is located at a distance of L/4 from the bottom of the tube (as shown in Fig. 1), the amplitude of pressure oscillations is maximized. This point corresponds to a peak modular product of pressure and velocity. In order to reconcile between former speculations and existing observations, a relation between acoustic heat, pressure, and velocity is suggested. This relation has the form [7]

$$\mathbf{q'} \sim p'\mathbf{u'}A,$$
 (8)

where A designates the flow cross-sectional area. In Eq. (8), the right-hand side, p'u', is known as the energy-flux vector. Its modulus represents the instantaneous energy flow per unit area for a given body of volume ϑ . Furthermore, the time average of this vector yields the acoustic intensity \overline{I} , the latter may be determined from

$$\overline{I} = \langle p' u' \rangle = \frac{1}{\tau} \int_0^{\tau} p' u' \, dt, \tag{9}$$

where integration is carried out over an oscillation period τ . Since the acoustic intensity \overline{I} retains dimensions of power per unit area, the integral of \overline{I} over a surface with unit normal n will constitute a measure of acoustic power across that surface, specifically,

$$\mathbb{P} = \int_{A} \langle p' \boldsymbol{u'} \cdot \boldsymbol{n} \rangle \, dA. \tag{10}$$

Based on energy conservation, it is therefore reasonable to suggest that, this acoustic energy per unit time that crosses a given flow area must originate from the thermal heat source energy, q'. On this note, a more refined expression relating thermodynamic variables may be proposed, namely,

$$\langle q' \rangle \sim \int_{A} \langle p' u' \cdot n \rangle \, dA.$$
 (11)

For a mathematical model that is dominated by the longitudinal velocity component u' (in the same direction as n), Eq. (11) becomes

$$\langle q' \rangle \sim \int_A \langle p' u' \, dA \rangle.$$
 (12)

Then, for a one-dimensional model, the acoustic pressure and velocity may be taken to be uniform along any cross-section. As such, one is left with

$$\langle q' \rangle \sim \langle p'u' \rangle A.$$
 (13)

This expression, proposed in previous work [64], agrees well with the relation derived recently by Yoon [65]. In fact, this form of acoustic energy flux also appears to have a substantial bearing on the onset of acoustic instability according to Sugimoto and Yoshida [66], Sugimoto et al. [67], and Biwa et al. [68], albeit entailing different solution domains.

B. Scaling Considerations

Since laboratory experimentation and numerical simulations tend to be time-intensive, it may be helpful to correlate measurements and computations in such a way to obtain the most information from the fewest experiments or computer runs. To this end, the tools of dimensional analysis may be applied to identify the group parameters that can promote a condition of similitude in a Rijke tube.

To begin, one may assume that heat oscillations can be influenced by a wide selection of variables. These include, but are not limited to: the pressure oscillation (p'), the longitudinal velocity oscillation (u'), the temperature oscillation (T'), the temperature difference measured from the heat source $(T_{hs} - T)$, the heat source location (x_{hs}) , the heat source diameter (d_{hs}) , and the Hertzian frequency of oscillations (f). Here the subscript "hs" denotes properties associated with the heat source element. In addition, we expect the viscosity (μ_0) , density (ρ_0) , specific heat (C_p) , heat transfer coefficient (h), speed of sound (a_0) , coefficient of thermal expansion (β_0) , gravitational constant (g_0) , tube length (L), tube diameter (D), and thermal conductivity (k_0) to be relevant. Note that the temperature difference can be perceived as the bulk difference between the warm and cold sections of the tube, following the analysis of Heckl and Howe [54]. In this context, the dependence of the dimensional heat oscillation on these parameters can be expressed as

$$q' = f(p', u', T', T_{hs} - T, x_{hs}, d_{hs}, f, \mu_0, \rho_0, C_p, h, a_0, L, D, k_0, \beta_0, g_0),$$
(14)

where the form of the function f is not yet known. After determining the rank of the dimensional matrix and applying the Buckingham-Pi theorem, one may choose p', u', T', and D as repeating parameters. Forthwith, fourteen Pi parameters emerge and these may be written as:

$$\Pi_{1} = \frac{q'}{p'u'D^{2}}, \ \Pi_{2} = \frac{\rho_{0}u'^{2}}{p'}, \ \Pi_{3} = \frac{C_{p}T'}{u'^{2}}, \ \Pi_{4} = \frac{fD}{u'}, \ \Pi_{5} = \frac{a_{0}}{u'}, \ \Pi_{6} = \frac{hT'}{p'u'}, \ \Pi_{7} = \frac{\mu_{0}u'}{p'D},$$

$$\Pi_{8} = \frac{x_{\rm hs}}{D}, \ \Pi_{9} = \frac{L}{D}, \ \Pi_{10} = \frac{d_{\rm hs}}{D}, \ \Pi_{11} = \frac{T_{\rm hs} - T}{T'}, \ \Pi_{12} = \frac{k_{0}T'}{p'u'D}, \ \Pi_{13} = \beta_{0}T', \ \text{and} \ \Pi_{14} = \frac{g_{0}D}{u'^{2}}.$$

As usual, these may be further rearranged into $\Pi_1 = F(\Pi_2, \Pi_3, \dots, \Pi_{14})$, or

$$\frac{q'}{p'u'D^2} = F\left[\frac{\rho_0 u'^2}{p'}, \frac{\rho_0 u'^2}{\rho_0 C_p T'}, \frac{fL}{a_0}, \frac{u'}{a_0}, \frac{hT'}{p'u'}, \frac{\mu_0 u'}{Dp'}, \frac{x_{\rm hs}}{L}, \frac{L}{D}, \frac{d_{\rm hs}}{D}, \frac{T_{\rm hs} - T}{T'}, \frac{k_0 T'}{p'u'D}, \beta_0 T', \frac{g_0 D}{u'^2}\right]. \tag{15}$$

Aside from the geometric scaling ratios, eleven specific groups may be identified:

The first, $\Pi_1 = q'/(p'u'D^2)$, defines a similarity grouping that relates the fluctuating heat flux to the acoustic pressure and velocity. It is perfectly consistent with Eq. (13).

The reciprocal of the second term, $p'/(\rho_0 u'^2) = Eu$, gives the ratio of the fluctuating thermodynamic and dynamic pressures associated with the acoustic field. It represents a form of the unsteady Euler number. However, since the unsteady Euler number is rarely utilized [69], one may apply scaling principles and replace Π_2 by Π_2/Π_7 , thus leading to the unsteady Reynolds number, $\Pi_2 = \rho_0 u' D/\mu_0 = Re$.

The third, $\Pi_3 = \rho_0 u'^2/(\rho_0 C_p T')$, yields the ratio of the dynamic pressure and the enthalpy of the acoustic field. This parameter can be alternatively written, through Π_{11} , as $u'^2/[C_p(T_{hs}-T)] = Ec$. This unsteady Eckert number gauges the fluctuating kinetic energy per unit sensible enthalpy.

The fourth, $\Pi_4 = f L/a_0 \sim n$, reflects a form of the Strouhal number based on the speed of sound. It actually returns the acoustic oscillation mode number. Recalling that, for an open-open tube at constant temperature, the frequency may be estimated from $f_n = na_0/(2L)$, Π_4 reduces to n/2, which scales with n.

The fifth, $\Pi_5 = u'/a_0 = Ma$, restores the unsteady Mach number.

The sixth, $\Pi_6 = hT'/(p'u')$, can be combined with Π_{12} , or $p'u' \sim k_0T'/D$, to recover the unsteady Nusselt number, $\Pi_6 = hD/k_0 = Nu$.

The seventh, $\Pi_7 = \mu_0 u'/(p'D) \sim (\mu_0 du'/dr)/p'$, provides a measure of the unsteady viscous shear relative to the acoustic pressure. This term can be further reduced using Π_{12} (or $p'u' \sim k_0 T'/D$), and Π_3 (or $T' \sim u'^2/C_p$), to deduce the unsteady Prandtl number, $\Pi_7 = \mu_0 u'^2/(p'u'D) = \mu_0 C_p/k_0 = Pr$.

The eighth, $\Pi_{11} = T'/(T_{hs} - T) = \theta$, refers to the so-called reduced temperature.

The ninth, $\Pi_{12} = k_0 T'/(p'u'D)$ or $\Pi_{12} = k_0 (T_{hs} - T)/(p'u'D)$, captures the ratio between unsteady heat conduction and the product of acoustic pressure and velocity. This term seems relevant to the computational work conducted by Farouk et al. [70], where the wall temperature is permitted to vary along two bounding walls.

The tenth term, $\beta_0 T'$, may be divided by the reduced temperature and written more conveniently as $\Pi_{13} = \beta_0 (T_{hs} - T)$, thus constituting a non-dimensional thermal expansion factor.

Lastly, the reciprocal of the eleventh term, $u'^2/(g_0D) = Fr$, returns the unsteady Froude number. However, given the more appreciable role of buoyancy in driving the naturally convected upward motion in a Rijke tube, this parameter may be multiplied by $\Pi_2^2\Pi_{13}$ and supplanted by the unsteady Grashof number, $\Pi_{14} = \rho_0 g_0 \beta_0 (T_{hs} - T) D^3/\mu_0^2 = Gr$.

At this juncture, Eq. (15) may be conveniently reduced to

$$\frac{q'}{p'u'D^2} = F\left[\frac{x_{\text{hs}}}{L}, \frac{L}{D}, \frac{d_{\text{hs}}}{D}, Re, Ec, n, Ma, Nu, Pr, \theta, \frac{k_0 T'}{p'u'D}, \beta_0(T_{\text{hs}} - T), Gr\right]. \tag{16}$$

Note that the form of Π_1 stands in perfect agreement with the proposed Eqs. (9) and (13) in Sec. III.A.

IV. Experimental Setup

A schematic of the Rijke tube, which is referred to in the experimental part of this study, is shown in Fig. 2. The setup consists of a simple cylindrical configuration that can be easily retrofitted. The actual apparatus comprises several modular two-inch nominal steel connectors. These interchangeable fittings are joined together by three-way tees, and the smaller side of each tee is attached to a short threaded connector, a reducer, a long threaded connector, and a cap for inserting a microphone [64].

The tube can be clamped either vertically or horizontally and its total length can be altered by replacing the connectors with either shorter or longer fittings. Due to the isobaric openings on both ends, the length of the tube corresponds to half of the fundamental oscillation wavelength, $\lambda_n = L/(2n)$, where n = 1 prescribes the first fundamental mode.

After introducing a heat source element at the critical location shown in Fig. 2, the magnitude and frequency of pressure oscillations are measured at four different locations along the tube. This is done by inserting "Realistic" microphones into the tees and connecting them to a two-channel HP-3582A spectrum analyzer. To protect each microphone from the rising pressures and temperatures in the tube, the microphone tips are inserted perpendicularly to the walls into the 15.24 cm (6") long connectors. This is done in order to, firstly, avoid introducing vortex shedding around the microphone tip [27]; secondly, reduce interference with measurements; and thirdly, provide a positive seal that prevents flow leakage past the microphone.

V. Computational Model

The unsteady flowfield evolving in a Rijke tube can be characterized using axisymmetric coordinates and a Navier–Stokes solver based on the volume of fluid (VOF) technique [71]. The VOF method consists of three elements: a scheme to locate the surface, an algorithm to track the surface, and a means of applying boundary conditions at the surface [72].

In the computational model, the tube length is set at 0.9 m and the internal diameter is chosen to be 0.05 m. Taking advantage of the prevailing axisymmetry, only one cross section of the tube needs to be modeled. Evidently, since the tube represents a body of revolution, material properties, boundary conditions, and other effects may be assumed to be axisymmetric relative to the centerline.

The computational mesh for the flow domain comprising the Rijke tube and its surroundings may be taken in a planar r-x slice as shown in Fig. 2. In this arrangement, a porous obstacle with a diameter of 3.75 cm may be inserted into the tube at a location of 22.5 cm from the bottom-end. This heating element is intended to mimic the behavior of a heat source. In this study, an obstacle porosity value of 0.9 is assigned to the heat source, thus implying a 90 percent

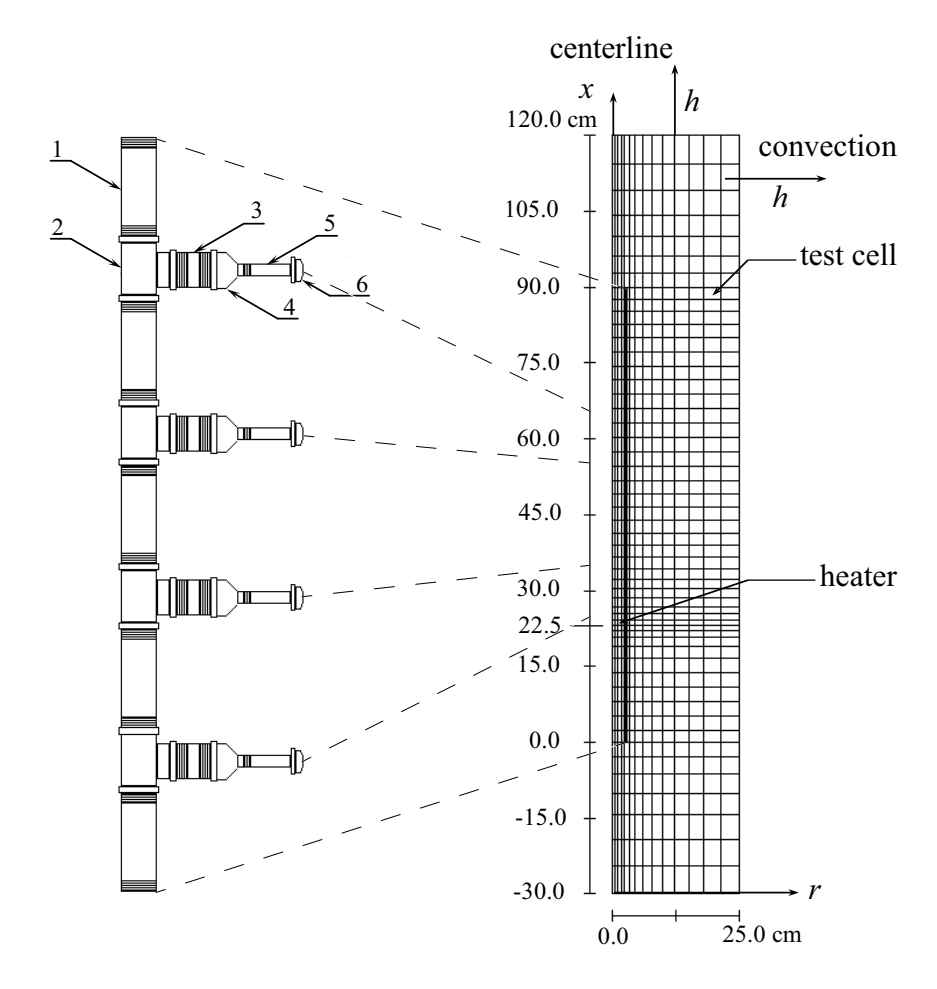


Fig. 2. Schematics of the experimental diagram of the Rijke tube apparatus [7] as well as the computational domain that includes the surrounding air volume. Items at left denote: i) the threaded connector section (2" nominal), ii) the tee section (2"×2"× $\frac{1}{2}$ "), iii) the short connector ($\frac{1}{2}$ " nominal), iv) the reducer ($\frac{1}{2}$ "× $\frac{1}{4}$ "), v) the long connector ($\frac{1}{4}$ "×12"), and vi) the cap ($\frac{1}{4}$ ").

Table 1. Experimental measurements at different Rijke tube locations.

-				
Ī	Microphone location from top outlet [cm]	SPL [dB]	p _{rms} [Pa]	f [Hz]
	65	134.5	108.3	248
	55	135.7	124.3	254
	35	135.6	122.9	246
	25	132.5	86.0	260

open area fraction. The thermal conductivity, density, and heat capacity of steel are used to prescribe the properties of the heating element. Finally, heat is released within the element over a finite length of time to avoid spurious errors that can occur when heat is released suddenly.

A. Heat Transfer Coefficients

Quasi-steady approximations of heat transfer coefficients are evaluated by the code using standard correlations for heat convection from flat surfaces. More specifically, the correlations are based on four thermal mechanisms: natural convection, forced laminar convection, forced turbulent convection, and conduction within the fluid. All correlations are evaluated and the largest value is automatically selected by the program.

B. Numerical Strategy

The numerical procedure is executed in two stages that take into account both transient and steady-state solution developments. The first stage carries the problem from an initial state of rest to a time of 20 seconds. At this point, the problem begins to exhibit limit-cycle oscillations that are characterized by nearly constant amplitudes.

The second stage carries the problem from 20 to 20.025 seconds over a much smaller time interval. This is done for the purpose of tracking more precisely the progressive acoustic wave growth. Meanwhile, virtual probes are located inside the simulated tube at several axial locations as shown graphically in Fig. 2. Numerically obtained pressures, temperatures, densities, and velocities are subsequently acquired and tabulated.

VI. Results and Discussion

A. Experimental Results

In the actual experiment, the heat source (here, a Bunsen burner) is mounted vertically inside the lower half of the tube. The burner heats the air around it, thus establishing a steady buoyancy-driven motion. The flame location is typically moved back and forth until an optimal position is found to excite most effectively the system's natural frequency. The level of acoustic growth is measured using a soundmeter and, as the flame is displaced, a loud and relatively pure tone is emitted and recorded by the microphones. This loud tone is continuously emitted as long as energy is supplied at the heater. One finds that the maximum sound pressure level is realized when the heater is located at L/4 from the bottom of the tube.

Acoustic oscillations diminish noticeably when the outflow area at the top is reduced or obstructed, and this behavior may be attributed to two primary factors. First, by constricting the outlet of the tube, equal and opposite (mirror) waves are produced that reflect back and forth at the tube's endwalls. This motion reduces the amplitude of acoustic oscillations. Second, by constricting the downstream end, the amount of air movement inside the tube is suppressed. This limits the convection heat transfer coefficient and reduces the thermoacoustic mode coupling.

In fact, a separate test may be used to verify that coupling with the naturally convected airflow is indeed a contributing factor to acoustic wave growth. This is accomplished by augmenting the air flowrate externally by means of a blower. When this is done, a higher intensity tone is emitted, which enables us to infer that forcing the air through the tube enhances the heat transfer coefficient and leads to a stronger acoustic environment.

The same experimental verification is then repeated in a Rijke tube held horizontally. Initially, using the standard configuration, oscillations do not occur when the tube is laid horizontally. This observation may be attributed to the absence of naturally convected flow, which is needed to promote thermoacoustic coupling. However, by adding a separate blower that forces air circulation, a sufficiently active convective motion is induced. This motion is

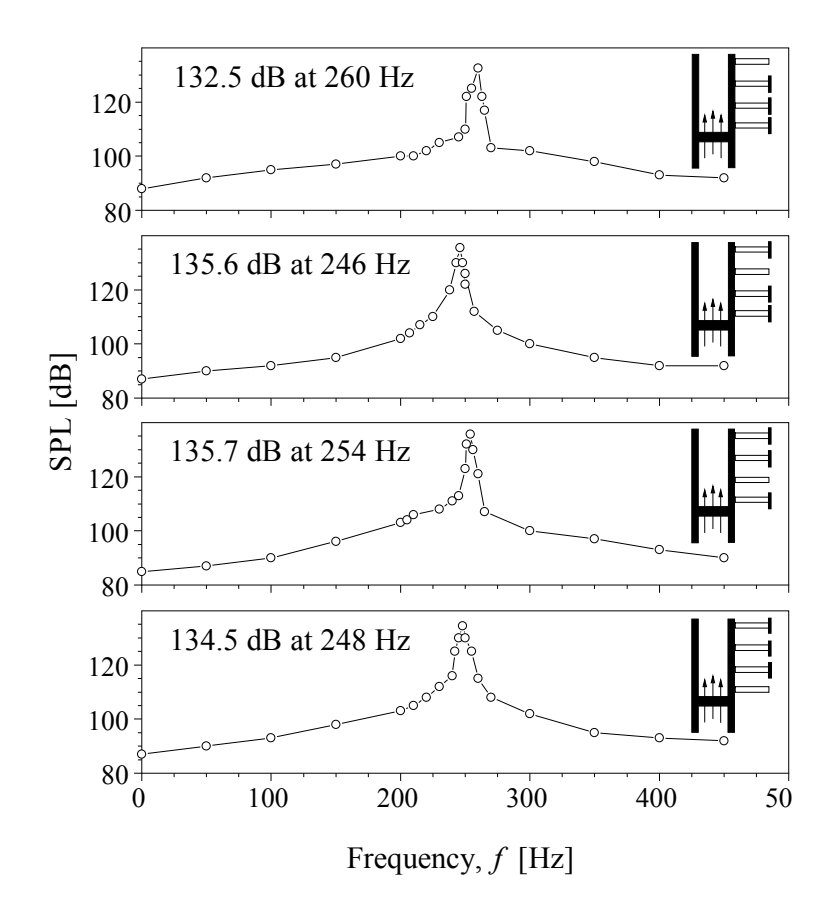


Fig. 3. Experimentally measured sound in the Rijke tube. From top to bottom, the microphone is located at 25, 35, 55, and 65 cm from the outlet section. The inset pinpoints the location of the microphone.

accompanied by a loud tone that is similar to that generated inside a naturally driven vertical tube.

Some experimental results are displayed in Fig. 3, where the amplitudes of the sound pressure level (SPL) are recorded at four different microphone locations taken along the tube. According to the spectrum analyzer used in this study, the frequency measurements are accompanied by a small uncertainty of $\pm 0.003\%$. In all four cases, heat addition is supplied at around L/4 from the bottom and the results are summarized in Table 1. Since the acoustic pressure amplitude peaks in the middle and vanishes at the open ends, the maximum SPL is recorded by the microphones that are closest to x = L/2.

In these runs, only the fundamental mode is excited at a frequency of approximately 250 Hz. This frequency corresponds to the finite length of the tube (L = 0.9 m). The small variations in frequency are due to the temperature fluctuations inside the tube during the test. A slight displacement of the heat source either downward or upward causes the amplitude to decrease. When the heat source is moved down to the x = L/8 position, the second mode (f = 500 Hz) is observed along with the first mode. This behavior is corroborated by Carvalho's experimental findings [73]. By the same token, moving the heat element to x = L/16 triggers the first three oscillation modes.

B. Computational Results

The computed pressure, axial velocity, and heat dissipation rate are illustrated in Fig. 4 for the first 20 seconds. It can be clearly seen that, after about 8.5 seconds, the pressure, velocity, and heat oscillations begin to occur. At this point in time, the temperature at the heater element would have reached its limit-cycle condition leading to constant amplitude oscillations. Given that the establishment of thermal fluctuations must necessarily precede the inception of strong pressure waves, the role of thermal oscillations in driving the acoustic motion may be readily inferred.

Following the first 20 seconds, Fig. 5 is used to illustrate the evolution of the pressure, axial velocity, and source-

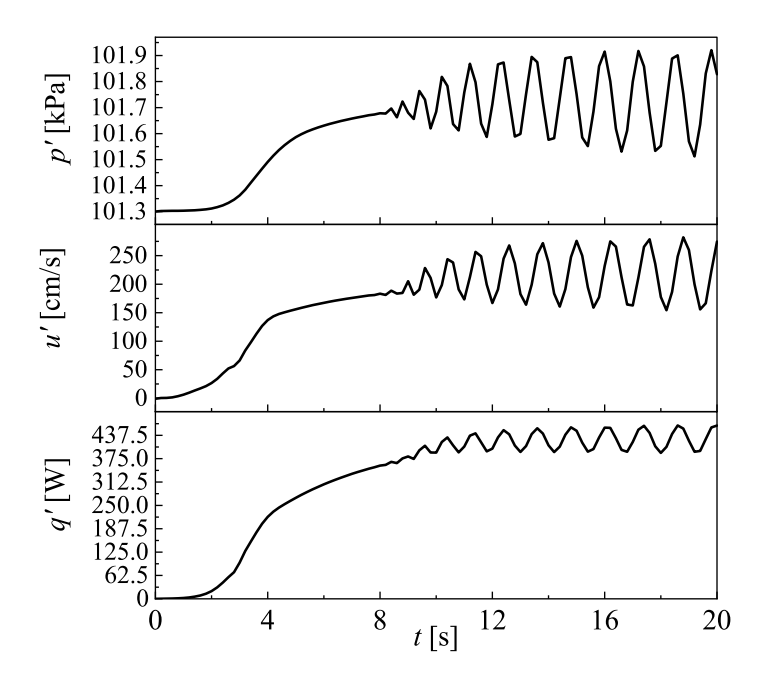


Fig. 4. Pressure, axial velocity, and heat release for the first 20.0 seconds. This is a standard run with 430 watts supplied to the heat source at x = L/4.

to-air heat transfer during the second stage. Here, a smaller time step is used in the simulations to track the acoustic wave growth more accurately. Based on the graph, one can infer that periodic oscillations are present in all of the variables with a frequency of about 200 Hz. This value falls within 19 percent of the analytical and experimental frequencies of 248 Hz. The former, which is given by $f_1 = a_0/(2L)$, is strongly dependent on the speed of sound approximation. The underlying discrepancy may be attributed to the specification of an overall lower temperature in the computational fluid dynamics (CFD) simulations compared to that affecting the experiments. In fact, a more precise evaluation of the speed of sound would require a weighted spatial integration over both cool and warm sections of the tube, i.e., by taking into account the spatial variation of the temperature. In our estimation, a global speed of sound of $a_0 \approx 331.2\sqrt{(T_{\rm avg} + 273.2)/273.2} \approx 447$ m/s, evaluated at an average temperature of $T_{\rm avg} \approx 225^{\circ}$ C, would be appropriate to use, as it would lead to a reconciliatory frequency of 248 Hz. In general, however, the use of a simple average that assumes a constant temperature will not be sufficient to fully characterize the problem [50]. Other methods that rely on a more detailed spatial average of the speed of sound across the tube will be later explored, and a discussion of the temperature profile on the resulting mode shapes and frequencies will be later entertained.

As described previously by Entezam et al. [74], a threshold value for heat input intensity must be exceeded before any appreciable acoustic coupling can be seen. The phase angle between acoustic pressure and fluctuating heat flux is also found to be 45°. In hindsight, the most significant result reported by Entezam et al. [74] may be the observation that maximum acoustic growth occurs when the energy heat flux vector is maximized. This observation lends support to the scaling analysis outlined in Sec. III.A.

In what regards proper heat source positioning, it is found that the spatial location of the heater element constitutes a key factor in producing thermoacoustic oscillations. When the source is placed in the lower half of the tube, large amplitude oscillations are reported. The resulting oscillations are found to exhibit their largest amplitudes when the source is located at precisely L/4 from the bottom. During separate runs, the source is relocated to both the middle (x = L/2) and upper (2L/3) sections of the tube, namely, to examine whether or not strong oscillations can be produced.

The numerical simulations confirm that when the source is positioned at L/2, the presence of an acoustic velocity node precludes the onset of oscillations. This observation stands in agreement with the arguments presented in Sec. III. The latter, let us recall, predict zero acoustic intensity at the chamber's mid-point. By the same token, a very weak signal is recorded when the source is placed at 2L/3. At that point, the oscillatory velocity and pressure are strictly out of phase. As a result, their potential to trigger acoustic excitation is drastically diminished.

Unsurprisingly, as the heat input is increased, the pressure oscillations are seen to grow progressively. Based on the

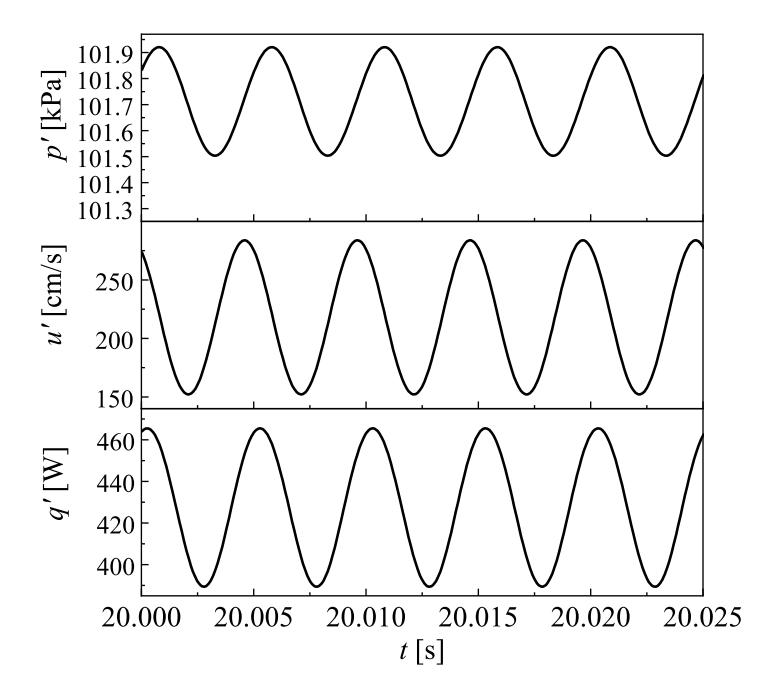


Fig. 5. Pressure, axial velocity, and heat release using a time step of 0.0025 seconds during limit-cycle oscillations.

data collected, a minimum value of heat addition appears to exist below which the thermoacoustic coupling becomes too weak to trigger any appreciable acoustic growth. When the heat input is sufficiently small, the acoustic sinks exceed the sources and acoustic attenuation prevails. Conversely, when the heat input is augmented beyond a critical threshold, acoustic sinks become insufficient and rapid acoustic amplification ensues. In our numerical simulation, this critical value is observed for a heater power supply of approximately $\mathbb{P}_{crit} \approx 430 \text{ W}$.

The computational work also shows that the modulus of heat transfer oscillations remains rather proportional to the modular product of acoustic velocity amplitude, acoustic pressure amplitude, and surface area of the heat source (see Fig. 6). This key result confirms the arguments leading to Eqs. (8), (13) and (16). In this vein, we find it useful to define the corresponding Rijke tube parameter as [69]

$$Rj \equiv \frac{q'}{p'u'D^2} \,, \tag{17}$$

where the symbol *Rj* is tentatively used in reference to Petrus (Pieter) Leonardus Rijke (1812-1899) for his brilliant discovery of the thermoacoustically generated sound through an open tube back in 1859[75]. Note that the sharp slopes that may be seen around 430 W in Fig. 6 suggest the presence of 'switching' or 'triggering.' Similar nonlinear jumps that can occur in thermacoustic devices are described by Noiray et al. [76], Noble et al. [77], and Sujith et al. [78].

To summarize, audible sound pressure oscillations will occur when the product of velocity and pressure fluctuations becomes sufficiently large at the location of the heat source, and will otherwise vanish when this product is suppressed. One also notes that, when the pressure and velocity fluctuations stay out of phase, the flow fluctuations will experience alternating pressure gradients that are continually unfavorable. This condition tends to suppress their motion and, in turn, the coupling with thermal oscillations at the heat source. These observations, first made speculatively, are now confirmed both numerically and experimentally. Moreover, they seem to agree with the interpretation offered by Raun et al. [6] concerning the effect of heat source positioning. Accordingly, "maximum driving occurs at the point a quarter of the way from the bottom of the tube where the product of the acoustic velocity and acoustic pressure has the maximum magnitude." Although they are stated differently, their conclusions support our observation that both pressure and velocity fluctuations must be appreciable and in phase for driving to occur. They also concur with both experimental and numerical findings suggesting that "driving does not occur if the gauze is placed at either a velocity or pressure node."

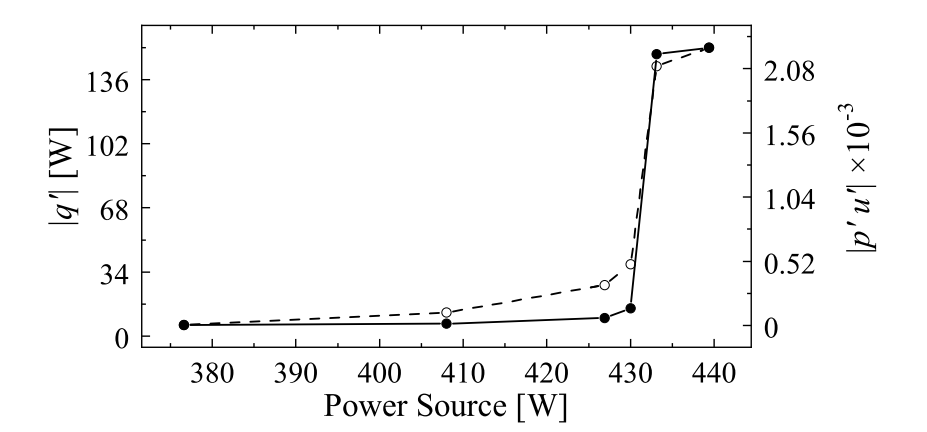


Fig. 6. Comparison between the modular product of acoustic pressure and velocity using solid circles (\bullet) , and the modulus of heat oscillations using hollow circles (\circ) .

VII. A Perturbative Approach

A. Basic Assumptions and Normalization

In this section, we initiate the development of an asymptotic procedure that takes into perspective some of the approximations used by the foregoing formulations. Although the different models that we have explored predict similar frequencies, the intent here is to pursue an alternative formulation that offers unique benefits and that may serve as an independent verification tool. For example, each of the Green's function and differential equation techniques make certain assumptions on the temperature variation within the tube. As such, it would be useful to examine the sensitivity of the ensuing oscillations to the spatial form of the temperature distribution. To do so, we shift our focus to a one-dimensional acoustics formulation that can accommodate an arbitrary axial temperature gradient along with an unsteady heat release function.

Based on a cursory review of the literature, it may be seen that several efforts have indeed been undertaken to combine these effects. One may cite, for example, the foundational work by Sujith et al. [79], Sujith [80], Sugimoto and Yoshida [66], Sugimoto et al. [67], Bednarik et al. [81], and Kumar and Sujith [82, 83], who have developed different analytical combinations of pressure and energy flux approximations for continuously varying temperature profiles. Assuming a linear temperature profile, Munjal and Prasad [84] have further managed to obtain a transfer matrix solution to the acoustic wave distribution in a pipe that combines the effects of the mean flow and temperature gradient. One may also pursue a WKB-type expansion for the acoustic field in ducted flows that are subject to an axial temperature gradient [85]. On this count, Li and Morgans [86] have constructed a WKB series for the acoustic motion in a duct given an arbitrary axial temperature gradient and mean flow; although the temperature gradient in their analysis is taken to be linear over small intervals, their solution is shown to be continually reliable and accurate over a wide range of Mach numbers. In the present investigation, however, it is desirable to account for a discontinuous thermal profile. For this reason, our objective will be directed toward the development of a semi-analytical formulation that is capable of accounting for the combined effects of an arbitrary temperature gradient and unsteady heat release on the pressure and, subsequently, the velocity field.

To set the stage, several assumptions are made. First, the flow in the Rijke tube is considered to be essentially one-dimensional, inviscid, and adiabatic, with constant thermophysical properties and no mean heat input or velocity. Furthermore, the air may be taken to be a perfect gas with a mean pressure that remains constant and a temperature distribution that depends solely on the axial coordinate. Although thermoacoustic instabilities are often accompanied by three disturbance modes [87], only the acoustic and entropic modes will be considered; the boundary-driven vortical mode will be neglected in view of the underlying inviscid and one-dimensional spatial assumptions. Under these auspices, the density may be related to two state properties, namely, the pressure and the specific entropy, s. Then,

using direct differentiation, one can split the material derivative of the density into

$$\frac{D\rho}{Dt} = \frac{\partial\rho}{\partial p} \Big|_{s} \frac{Dp}{Dt} + \frac{\partial\rho}{\partial s} \Big|_{p} \frac{Ds}{Dt} = \frac{1}{a_{0}^{2}} \frac{Dp}{Dt} + \frac{\partial\rho}{\partial s} \Big|_{p} \frac{Ds}{Dt}$$
 (18)

Furthermore, by dismissing viscous dissipation and heat conduction, one may follow Dowling [88] and write, for an ideal gas,

$$\frac{D\rho}{Dt} = \frac{1}{a_0^2} \left[\frac{Dp}{\partial t} - (\gamma - 1) \, q_{\,\theta} \right],\tag{19}$$

where q_{ϑ} denotes the total heat release rate per unit volume. The resulting expression can be further simplified for the case of negligible mean flow. One gets

$$\frac{D\rho}{Dt} = \frac{1}{a_0^2} \left[\frac{\partial p'}{\partial t} - (\gamma - 1) \, q'_{\vartheta} \right],\tag{20}$$

with q'_{θ} denoting the fluctuating heat release rate per unit volume. At this juncture, the velocity and pressure disturbances may be taken to be small, in conformance with the theory of linear acoustics. This enables us to decompose the instantaneous variables into mean and fluctuating quantities, namely, $p = p_0 + p'$, $\rho = \rho_0 + \rho'$, and u = u'. As usual, this decomposition allows us to linearize the mass and momentum equations and recover their standard acoustic forms [89],

$$\frac{D\rho}{Dt} + \rho_0 \nabla \cdot \mathbf{u}' = 0 \quad \text{(mass conservation)},\tag{21}$$

and

$$\frac{\partial u'}{\partial t} + \frac{\nabla p'}{\rho_0} = 0 \quad \text{(momentum conservation)}. \tag{22}$$

Next, the dimensional pressure and velocity perturbation equations may be derived. This is done by combining Eqs. (20–22) with the ideal gas equation, $p_0 = \rho_0 R T_0$, and expanding the derivatives in one-dimensional space. One obtains

$$\frac{\partial^2 p'}{\partial t^2} - a_0^2 \frac{\partial^2 p'}{\partial x^2} = \gamma R \frac{dT_0}{dx} \frac{\partial p'}{\partial x} + (\gamma - 1) \frac{\partial q'_{\vartheta}}{\partial t}, \tag{23}$$

and

$$\frac{\partial^{2} u'}{\partial t^{2}} - a_{0}^{2} \frac{\partial^{2} u'}{\partial x^{2}} = -\gamma R \frac{\mathrm{d} T_{0}}{\mathrm{d} x} \frac{\partial u'}{\partial x} - \frac{R}{p_{0}} \left[\frac{\mathrm{d} T_{0}}{\mathrm{d} x} \frac{\partial p'}{\partial t} - (\gamma - 1) \frac{\mathrm{d} T_{0}}{\mathrm{d} x} q'_{\vartheta} + (\gamma - 1) T_{0} \frac{\partial q'_{\vartheta}}{\partial x} \right]$$
(24)

It may be helpful to note several characteristic properties in these coupled relations. First, in reference to the pressure wave equation given by Eq. (23), the axial temperature gradient can modify the first derivative of the pressure by virtue of its role as the coefficient of the pressure gradient on the right-hand-side. It can effectively serve as either a driver or inhibitor depending on its sign; in fact, this functionality will become apparent once the perturbed expansion for the pressure approximation is complete. Second, the derivative of the heat release in Eq. (23) is clearly seen to act as a source of pressure waves. Third, in regards to the velocity wave equation given by Eq. (24), several effects may be inferred. When the axial temperature gradient acts as a driver of pressure oscillations in Eq. (23), it becomes a dissipator of acoustic velocity oscillations by virtue of the sign switch that its coefficient undergoes in Eq. (24). Fourth, the time-dependent pressure disturbance gradient may be seen to function as a sink of acoustic velocity waves so long as the axial temperature gradient remains positive. This confirms that, when the pressure oscillations increase with the passage of time, the velocity oscillations decrease, namely, as one would expect from their 90° phase difference. If we were to track a discrete packet of molecules that cross the heater element, the volume of this packet would greatly expand. Assuming that the internal domain can be readily divided into two distinct temperature zones, the region above the heater will then exhibit a higher temperature and so, by applying Boyle's law, a change in volume will directly induce a change in pressure. Lastly, the unsteady temperature and heat oscillations may be seen to function as sources (or sinks) of acoustic velocity waves. In fact, the accurate specification of the axial temperature gradient along the tube may be well justified given its strong bearing on the system's wave dynamics. In contrast, higher-order temperature derivatives do not appear to be consequential in the linear regime.

At this stage, it will be helpful to normalize our principal equations in Eqs. (23) and (24), starting with their basic spatial and temporal coordinates. We proceed by taking

$$\tilde{p} = \frac{p'}{p_0}$$
, $\tilde{t} = \omega_0 t$, $\tilde{u} = \frac{u'}{(a_0)_{\min}}$, $\tilde{x} = \frac{x}{L}$, $\tilde{T}_0 = \frac{T_0}{(T_0)_{\min}}$, $\tilde{q} = \frac{q'_{\theta} L}{p_0(a_0)_{\min}}$, and $\omega_0 = \frac{(a_0)_{\min}}{L}$, (25)

where the tildes denote dimensionless quantities and ω_0 represents the characteristic normalizing frequency, not to be confused with the first fundamental mode; the latter is labeled either ω_1 or f_1 depending on whether it refers to the circular or Hertzian frequency. These, in turn, may be normalized using $\tilde{\omega}_1 = \omega_1/\omega_0$ and $\tilde{f}_1 = f_1/\omega_0$, respectively. In the above, the subscript "min" refers to the minimum value of a given property taken along the coldest section of the tube, which typically occurs at entry. Note that, in mimicking the heat release law, the unsteady heat release, q'_{ϑ} , is normalized using the characteristic pressure, velocity, and length. By substituting these normalizing expressions into Eqs. (23) and (24), one arrives at the following non-dimensional set:

$$\frac{\partial^2 \tilde{p}}{\partial \tilde{t}^2} - \tilde{T}_0 \frac{\partial^2 \tilde{p}}{\partial \tilde{x}^2} = \frac{d\tilde{T}_0}{d\tilde{x}} \frac{\partial \tilde{p}}{\partial \tilde{x}} + (\gamma - 1) \frac{\partial \tilde{q}}{\partial \tilde{t}}, \qquad (26)$$

and

$$\frac{\partial^2 \tilde{u}}{\partial \tilde{t}^2} - \tilde{T}_0 \frac{\partial^2 \tilde{u}}{\partial \tilde{x}^2} = -\frac{\mathrm{d} \tilde{T}_0}{\mathrm{d} \tilde{x}} \frac{\partial \tilde{u}}{\partial \tilde{x}} - \frac{1}{\gamma} \frac{\mathrm{d} \tilde{T}_0}{\mathrm{d} \tilde{x}} \frac{\partial \tilde{p}}{\partial \tilde{t}} - \frac{\gamma - 1}{\gamma} \left(\tilde{T}_0 \frac{\partial \tilde{q}}{\partial \tilde{x}} - \tilde{q} \frac{\mathrm{d} \tilde{T}_0}{\mathrm{d} \tilde{x}} \right). \tag{27}$$

To make further headway, we find it useful to define the naturally occurring small parameter, $\varepsilon \equiv (\gamma - 1)/\gamma$, at the basis of our asymptotic expansion approach. This perturbation parameter enables us to capture the effect of the temperature variation on the pressure and velocity disturbances while treating it as a primary contributor. It will also enable us to incorporate the unsteady heat release effect as a secondary contributor, i.e., owing to the size of ε and assuming small deviations from linearity.

B. Leading-Order Perturbation Expansion

Noting that $\gamma = 1/(1 - \varepsilon) = O(1)$, Eqs. (26) and (27) may be reduced to:

$$\frac{\partial^2 \tilde{p}}{\partial \tilde{t}^2} - \tilde{T}_0 \frac{\partial^2 \tilde{p}}{\partial \tilde{x}^2} = \frac{d\tilde{T}_0}{d\tilde{x}} \frac{\partial \tilde{p}}{\partial \tilde{x}} + \varepsilon \gamma \frac{\partial \tilde{q}}{\partial \tilde{t}} , \qquad (28)$$

and

$$\frac{\partial^2 \tilde{u}}{\partial \tilde{t}^2} - \tilde{T}_0 \frac{\partial^2 \tilde{u}}{\partial \tilde{x}^2} = -\frac{d\tilde{T}_0}{d\tilde{x}} \frac{\partial \tilde{u}}{\partial \tilde{x}} - (1 - \varepsilon) \frac{d\tilde{T}_0}{d\tilde{x}} \frac{\partial \tilde{p}}{\partial \tilde{t}} - \varepsilon \left(\tilde{T}_0 \frac{\partial \tilde{q}}{\partial \tilde{x}} - \tilde{q} \frac{d\tilde{T}_0}{d\tilde{x}} \right). \tag{29}$$

Clearly, the perturbation decomposition incorporates the effects of the temperature gradient at the leading order while deferring those of the unsteady heat release to the first order in ε . As usual, the solution may be reconstructed using $\tilde{p} = \tilde{p}^{(0)} + \varepsilon \tilde{p}^{(1)} + O(\varepsilon^2)$ and $\tilde{u} = \tilde{u}^{(0)} + \varepsilon \tilde{u}^{(1)} + O(\varepsilon^2)$, where the superscript refers to the perturbation order. At the leading order, it is not necessary to specify \tilde{q} ; the latter can be left as a placeholder that serves to accommodate a user-defined heat release law, such as Eq. (8) or, alternatively, a particular flame transfer or a flame describing function.

1. Leading-Order Equation Type

The leading-order approximation examines the effect of a purely axial temperature gradient with no direct participation from the unsteady heat release. The axial temperature can be taken to be an arbitrary function of \tilde{x} with at least a continuous first derivative. Using the decomposed variables and letting $\varepsilon \to 0$, Eqs. (28) and (29) render the sequentially coupled set,

$$\frac{\partial^2 \tilde{p}^{(0)}}{\partial \tilde{t}^2} = \tilde{T}_0 \frac{\partial^2 \tilde{p}^{(0)}}{\partial \tilde{x}^2} + \frac{d\tilde{T}_0}{d\tilde{x}} \frac{\partial \tilde{p}^{(0)}}{\partial \tilde{x}} , \qquad (30)$$

with

$$\frac{\partial^2 \tilde{u}^{(0)}}{\partial \tilde{t}^2} = \tilde{T}_0 \frac{\partial^2 \tilde{u}^{(0)}}{\partial \tilde{x}^2} - \frac{d\tilde{T}_0}{d\tilde{x}} \frac{\partial \tilde{u}^{(0)}}{\partial \tilde{x}} - \frac{d\tilde{T}_0}{d\tilde{x}} \frac{\partial \tilde{p}^{(0)}}{\partial \tilde{t}} . \tag{31}$$

It should be noted at this point that the solution of Eq. (31) depends on $\tilde{p}^{(0)}$, and that the leading-order pressure wave is retrievable directly from Eq. (30). Procedurally, it may be helpful to recognize that Eqs. (30) and (31) exhibit the canonical form

$$\frac{\partial^2 w}{\partial t^2} = f(x) \frac{\partial^2 w}{\partial x^2} + g(x) \frac{\partial w}{\partial x} + \phi(x, t). \tag{32}$$

Using the identity provided in Section 4.5.3-3 of Polyanin [90], one may readily group congruent terms and write

$$\frac{\partial^2 \tilde{p}^{(0)}}{\partial \tilde{t}^2} = \frac{\partial}{\partial \tilde{x}} \left(\tilde{T}_0 \frac{\partial \tilde{p}^{(0)}}{\partial \tilde{x}} \right),\tag{33}$$

with

$$\frac{1}{\tilde{T}_0^2} \frac{\partial^2 \tilde{u}^{(0)}}{\partial \tilde{t}^2} = \frac{\partial}{\partial \tilde{x}} \left(\frac{1}{\tilde{T}_0} \frac{\partial \tilde{u}^{(0)}}{\partial \tilde{x}} \right) - \frac{1}{\tilde{T}_0^2} \frac{d\tilde{T}_0}{d\tilde{x}} \frac{\partial \tilde{p}^{(0)}}{\partial \tilde{t}} . \tag{34}$$

We thus recover a modified wave equation that embodies the temperature distribution and its gradient explicitly. As for the last term in Eq. (34), it corresponds to the arbitrary source term $\phi(x, t)$ in Eq. (32).

Fortuitously, a general solution for each of the transformed equations can be obtained based on a Green's function and a Sturm-Liouville eigenvalue solver [90]. A Green's function expression is reassuring because a similar formulation is used by Bigongiari and Heckl [53] to account for the presence of unsteady heat release and a piecewise axial temperature. In fact, having procedurally identified a general solution form, we may proceed to define suitable boundary conditions. Specifically, we may equate the characteristic length, L, to the Rijke tube's, and assign pressure nodes and velocity antinodes to the tube's endwalls. As for the unsteady heat source, it may be expressed using a Dirac delta function at $\tilde{x} = 1/4$.

2. Leading-Order Fluctuating Pressure Approximation

The boundary and initial conditions on Eq. (33) may be specified as:

$$\tilde{p}^{(0)} = 0 \quad \text{at} \quad \tilde{x} = 0,$$

$$\tilde{p}^{(0)} = 0 \quad \text{at} \quad \tilde{x} = 1,$$

$$\tilde{p}^{(0)} = f_p(\tilde{x}) \quad \text{at} \quad \tilde{t} = 0,$$

$$\frac{\partial \tilde{p}^{(0)}}{\partial \tilde{t}} = g_p(\tilde{x}) \quad \text{at} \quad \tilde{t} = 0,$$

$$(35)$$

where f_p and g_p designate the initial spatial distribution of the pressure wave throughout the tube along with its time-derivative. Although a general solution to the resulting set is possible, the formulation that takes into account these physical requirements leads to a Sturm-Liouville problem [90]. In the interest of simplicity, an asymptotic approximation to the resulting set will be pursued.

To start, it may be recognized that the solution for Eq. (33) yields

$$\tilde{p}^{(0)} = \frac{\partial}{\partial \tilde{t}} \left(\int_0^1 f_p(\xi) G_p(\tilde{x}, \xi, \tilde{t}) \, \mathrm{d}\xi \right) + \int_0^1 g_p(\xi) G_p(\tilde{x}, \xi, \tilde{t}) \, \mathrm{d}\xi, \tag{36}$$

where

$$G_p(\tilde{x}, \xi, \tilde{t}) = \sum_{n=1}^{\infty} \frac{y_n(\tilde{x})y_n(\xi)}{\|y_n\|^2} \frac{\sin(\tilde{\omega}_n \tilde{t})}{\tilde{\omega}_n}; \quad \|y_n\|^2 = \int_0^1 y_n^2(\tilde{x}) \, \mathrm{d}\tilde{x}. \tag{37}$$

Here, G_p represents the Green's function for the pressure wave, which allows the two initial pressure-related distributions to propagate over the solution domain. It comprises both $\tilde{\omega}_n$ and $y_n(\tilde{x})$, the eigenvalue and eigenfunction of the Sturm-Liouville problem for the pressure. In this particular problem, we recall that the latter exhibits infinitely many positive definite and distinct eigenvalues. Moreover, the spatial solution to Eq. (33) for the pressure mode shape can be written in the standard Sturm-Liouville form, namely,

$$\frac{\mathrm{d}}{\mathrm{d}\tilde{x}} \left[\tilde{T}_0(\tilde{x}) \frac{\mathrm{d}y_n(\tilde{x})}{\mathrm{d}\tilde{x}} \right] + \tilde{\omega}_n^2 y_n(\tilde{x}) = 0, \tag{38}$$

with $y_n(0) = y_n(1) = 0$. The resulting homogenous problem can be solved either computationally for the appropriate eigenvalues and eigenfunctions, or asymptotically, which will be the avenue undertaken here.

It may be useful to remark that despite the infinite summation in Eq. (37), the solution remains dominated by the first set of eigenmodes; the contributions of the higher eigenmodes become increasingly smaller, as one may infer from the squeeze theorem. Accordingly, we have

$$\lim_{\tilde{\omega}_n \to \infty} \frac{\sin(\tilde{\omega}_n)}{\tilde{\omega}_n} = 0, \quad \lim_{\tilde{\omega}_n \to \infty} \frac{\sin(\tilde{\omega}_n \tilde{t})}{\tilde{\omega}_n} = 0; \ \forall \tilde{t} > 0, \tag{39}$$

$$\lim_{\tilde{\omega}_n \to 0} \frac{\sin(\tilde{\omega}_n)}{\tilde{\omega}_n} = 1, \quad \text{and} \quad \lim_{\tilde{\omega}_n \to 0} \frac{\sin(\tilde{\omega}_n \tilde{t})}{\tilde{\omega}_n} = \tilde{t}; \ \forall \tilde{t} > 0.$$

$$(40)$$

American Institute of Aeronautics and Astronautics

The corresponding term in Eq. (37) will clearly dominate at low frequencies irrespective of time, becoming progressively less appreciable with successive increases in $\tilde{\omega}_n$.

Interestingly, for $n \gg 1$, the eigenvalues and respective eigenfunctions can be approximated, thus leading to a more compact asymptotic solution. Physically, the $n \gg 1$ condition occurs when all of the modes in the tube are accounted for and superimposed. At the outset, the following modal waveforms may be specified:

$$\frac{y_n(\tilde{x})}{\|y_n\|} = \left[\frac{4}{\tilde{T}_0(\tilde{x})\Theta^2}\right]^{1/4} \sin\left[\frac{\pi n}{\Theta} \int_0^{\tilde{x}} \frac{1}{\sqrt{\tilde{T}_0(\tilde{x})}} d\tilde{x}\right] + O\left(\frac{1}{n}\right);$$

$$\Theta \equiv \int_0^1 \frac{1}{\sqrt{\tilde{T}_0(\tilde{x})}} d\tilde{x} \quad \text{and} \quad \tilde{\omega}_n \approx \frac{\pi n}{\Theta} .$$
(41)

Hence, by combining these asymptotic expressions with the Green's function formulation, the leading-order solution for the pressure can be fully identified. It may be helpful to remark that this solution can accommodate an arbitrary temperature distribution within a tube given a well-prescribed nodal pressure condition at both endwalls.

To make further headway, it may be helpful to recognize that, since both integrals in Eq. (36) are defined over the same domain, and granted that the initial pressure distribution remains time invariant, the two integrals may be readily combined using the Leibniz rule and rearranged into

$$\tilde{p}^{(0)} = \int_0^1 \left[f_p(\xi) \frac{\partial G_p(\tilde{x}, \xi, \tilde{t})}{\partial \tilde{t}} + g_p(\xi) G_p(\tilde{x}, \xi, \tilde{t}) \right] d\xi \,. \tag{42}$$

Subsequently, by substituting Eq. (37) into Eq. (42), one obtains,

$$\tilde{p}^{(0)} = \sum_{n=1}^{\infty} \frac{y_n(\tilde{x})}{\|y_n\|} \left[\cos\left(\tilde{\omega}_n \tilde{t}\right) \int_0^1 \frac{y_n(\xi)}{\|y_n\|} f_p(\xi) \, \mathrm{d}\xi + \frac{1}{\tilde{\omega}_n} \sin\left(\tilde{\omega}_n \tilde{t}\right) \int_0^1 \frac{y_n(\xi)}{\|y_n\|} g_p(\xi) \, \mathrm{d}\xi \right] . \tag{43}$$

We thus arrive at a closed-form asymptotic solution for the pressure waveform given an arbitrary temperature distribution, $\tilde{T}_0(\tilde{x})$. This expression enables us to predict the time-evolution of the pressure mode shapes for a user-specified thermal profile through direct integration; in short, it obviates the need to solve modal differential equations. Its accuracy will be further examined in an upcoming comparison with a differential equation formulation developed by Sujith [79].

At this juncture, several useful insights may be inferred from the resulting formulation. On the one hand, assuming a purely isentropic solution at leading order, one recovers strictly acoustic, inviscid, and irrotational waves that do not exhibit any vortical or entropic disturbance effects. This behavior may be expected because the presence of vortical waves is excluded by virtue of the inviscid and quiescent flow assumptions. On the other hand, the acoustic mode shape, frequency, and speed of propagation appear to be primarily influenced by the mean temperature distribution and its time-derivative. Lastly, the asymptotic formulation may be seen to produce closed-form expressions over a wide selection of thermal profiles as long as the $1/\sqrt{\tilde{T}_0(\tilde{x})}$ term can be analytically integrated. Otherwise, numerical computations must be carried out, thus leading to a semi-analytical approximation. In what follows, we show that Eq. (43) can be readily evaluated for a variety of thermal profiles.

C. Acoustic Pressure for a Prescribed Temperature Distribution

By way of verification, several thermal profiles will be used to evaluate the resulting pressure distribution. These start with uniform and linearly increasing or decreasing thermal profiles and, as depicted in Table 2, extend to nonlinear distributions that include quadratic, exponential, and sinusoidal profiles. For added clarity, these 10 basic patterns are regrouped and illustrated in Fig. 7. Note that $\tilde{T}_0(\tilde{x})$ can consist of any combination of these analytical functions, which are defined over a unitary interval of [1, 2], except for the uniform profile; it may be further expressed in terms of data measurements or computed predictions based on actual or simulated thermoacoustic environments. In practice, because of the upward direction of natural convection, the temperature in a Rijke tube will typically remain fairly constant in the cold segment below the heat source, and then switch to an exponentially decaying function in the hot segment [7]. This particular behavior will be separately examined in Sec. VII.C.3. In fact, other attempts to determine the pressure wave for a given temperature field have already been pursued in the literature; for example, Bednarik et al. [81] rely on Heun's equation, while Li and Morgans [86] employ a linearized approximation of an arbitrary temperature

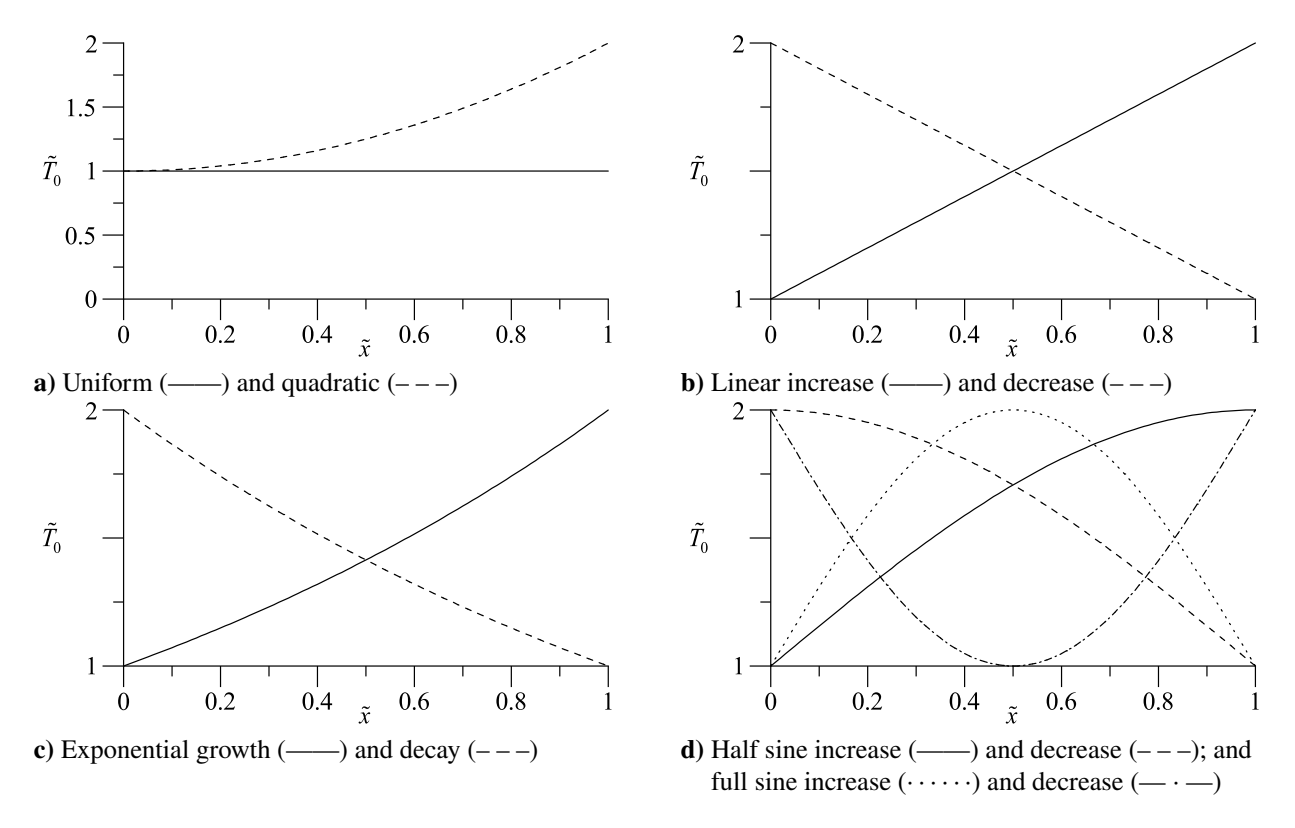


Fig. 7. Thermal profiles corresponding to Table 2 for spatial distributions that are a) uniform and quadratic, b) linearly increasing and decreasing, c) exponentially increasing and decreasing, and d) sinusoidally increasing and decreasing both with half and full periods.

Table 2. Non-dimensional temperature distributions used in the leading-order pressure approximations.

Туре	Mean temperature, $\tilde{T}_0(\tilde{x})$	Physical characteristics
Constant	$\tilde{T}_0(\tilde{x}) = 1$	Maintains uniform temperature throughout
Linearly increasing	$\tilde{T}_0(\tilde{x}) = 1 + \tilde{x}$	Corroborates case based on Sujith et al. [79]
Linearly decreasing	$\tilde{T}_0(\tilde{x}) = 2 - \tilde{x}$	Corroborates case based on Sujith et al. [79]
Quadratic (nonlinear)	$\tilde{T}_0(\tilde{x}) = 1 + \tilde{x}^2$	Captures concave up thermal increase
Exponentially increasing	$\tilde{T}_0(\tilde{x}) = e^{\tilde{x} \ln 2}$	Mimics thermal profile below heat source
Exponentially decreasing	$\tilde{T}_0(\tilde{x}) = 2e^{-\tilde{x}\ln 2}$	Mimics thermal profile above heat source
Sinusoidally increasing (half period)	$\tilde{T}_0(\tilde{x}) = 1 + \sin(\pi \tilde{x}/2)$	Captures concave down thermal increase
Sinusoidally decreasing (half period)	$\tilde{T}_0(\tilde{x}) = 1 + \cos(\pi \tilde{x}/2)$	Captures concave down thermal decrease
Sinusoidally increasing (full period)	$\tilde{T}_0(\tilde{x}) = 1 + \sin(\pi \tilde{x})$	Mimics increasing temperature off endwalls
Sinusoidally decreasing (full period)	$\tilde{T}_0(\tilde{x}) = 2 - \sin(\pi \tilde{x})$	Mimics decreasing temperature off endwalls

distribution. Presently, the Green's function formulation will be used at the basis of predicting the pressure waveform. For all test cases considered, the solution is evaluated based on the first 50 eigenvalues, although a smaller number of terms can be used to speed up computations. The initial distributions are set equal to $f_p = y_n(\tilde{x})/\|y_n\|$, where n specifies the acoustic mode to be captured, normalized such that the maximum value of f_p is unity; we also take $g_D = 0$, as these conditions reflect the expected acoustic waveform for a given thermal profile. For example, in the case of a uniform temperature, the use of $\tilde{T}_0(\tilde{x}) = 1$ leads to the well-known sinusoidal pressure waveform, $f_D = \sin(\pi \tilde{x})$, in a quiescent tube.

Forthwith, solutions for different thermal profiles are generated and displayed in Fig. 8 through Fig. 11. Note that full lines are used to demarcate the mode shape envelope by outlining its borders; in this context, broken lines are used to represent evenly incremented timelines that proceed from the initial pressure modal line to the lowest trough over half a period; on the other hand, hollow circles are used to represent the returning motion from the lowest trough to the highest peak. Being separated by an equal fraction of the oscillation period, the timelines may be seen to overlap on their way back, while the pressure peaks remain stationary, as expected of standing waveforms.

1. Effects of Uniform, Linear, and Quadratic Temperature Distributions

The first test case corresponds to a constant temperature throughout the tube. In an open-open configuration, one expects the pressure to resemble a conventional sinusoidal wave. This isothermal condition can be simulated by letting $T_0 = 1$. Then based on Eq. (43), $\tilde{p}^{(0)}$ may be evaluated with a time step of $\tilde{\tau}_n/12$, where $\tilde{\tau}_n = \tau_n \omega_0 = 2\pi/\tilde{\omega}_n$ denotes the non-dimensional modal period for one cycle. This periodic designation will be implemented everywhere unless specified otherwise. The corresponding timelines, which are evenly spaced in time, are displayed in Fig. 8a; these start with the initial sinusoidal distribution, and end after one full cycle, with the final standing wave structure depicting a stationary maximum amplitude.

It may be clearly seen from the resulting mode shape in Fig. 8a that we readily recover the sinusoidal pattern associated with a standing wave in an open-open tube occupied by an isothermal fluid. The observed wave behavior is consistent with acoustic theory and can thus be viewed as a limiting process verification of the underlying framework.

In addition to the uniform profile, a quadratic temperature distribution may be examined using $\tilde{T}_0(\tilde{x}) = 1 + \tilde{x}^2$; the outcome is displayed side-by-side to the case of $\tilde{T}_0(\tilde{x}) = 1$ in Fig. 8b. Although the pressure nodes and antinodes remain stationary, the skewed thermal profile causes the antinodes to shift leftward and closer to the tube's entrance, namely, to $\tilde{x}_{max} \approx 0.4378$, where the subscript marks the peak pressure location. Although the timelines remain symmetrical over a cycle, their peak values no longer coincide with the midpoint of the tube; they move closer to the coldest point in the chamber due to the faster speed of sound in the top portion of the tube, i.e., where the temperature is increasingly higher. This particular nodal shifting can be explained as follows: Since the speed of propagation is lower near $\tilde{x} = 0$ and higher near $\tilde{x} = 1$, the right (upward) traveling wave becomes slower in the upstream section of the tube and faster downstream; similarly, the left (downward) traveling wave becomes faster near the top and slower near the bottom. This spatial imbalance in propagation speed of the two traveling waves leads to a leftward shift in the peak value of their consolidated mode shapes, whose superposition determines the standing wave structure.

The next test cases that we consider correspond to the linearly increasing and decreasing temperature profiles, $\tilde{T}_0(\tilde{x}) = 1 + \tilde{x}$ and $\tilde{T}_0(\tilde{x}) = 2 - \tilde{x}$, respectively. These enable us to identify the effects of positive and negative temperature gradients on the character of the pressure waveform. They also allow us to verify the present formulation

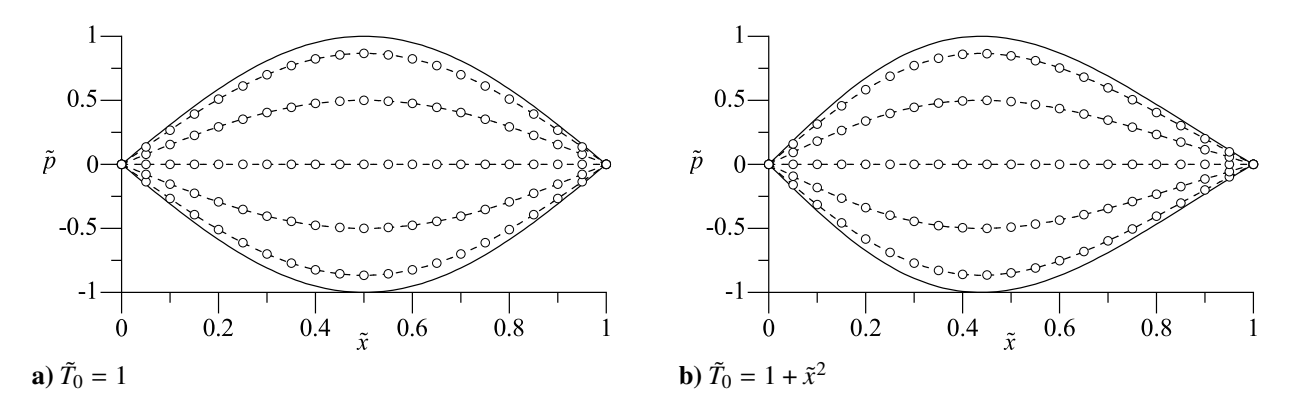


Fig. 8. Acoustic pressure variations corresponding to (a) constant mean temperature and (b) quadratic mean temperature profiles. Unless specified otherwise, full lines (——) demarcate the mode shape envelope whereas broken lines (– –) and hollow circles (\circ) represent evenly incremented timelines, taken every $\tilde{\tau}_n/12 = \pi/(6\tilde{\omega}_n)$, over the first and second half periods, respectively.

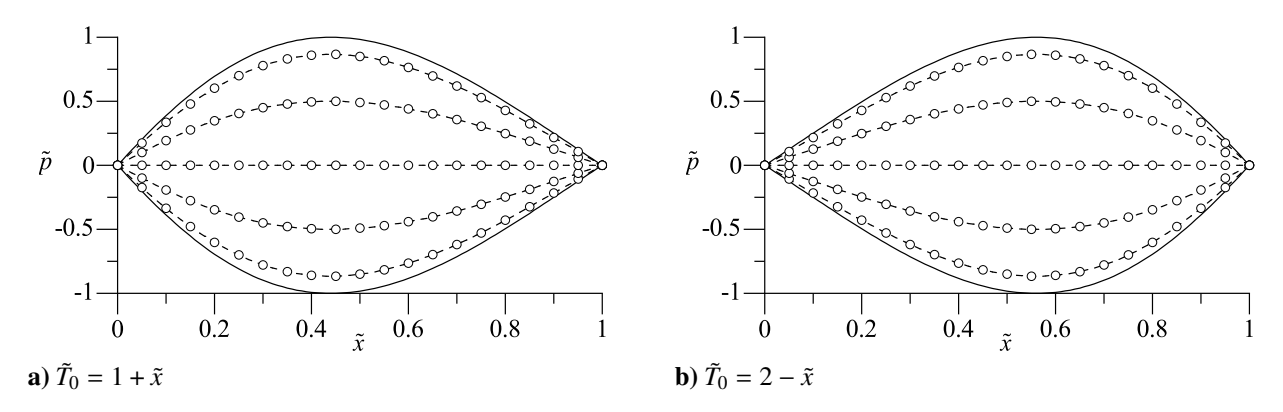


Fig. 9. Acoustic pressure variations corresponding to (a) linearly increasing and (b) linearly decreasing mean temperature profiles.

by facilitating comparisons to the predictions of Sujith et al. [79]; the latter investigate the behavior of linear temperature distributions in ducts using a transformed wave equation that can be reduced to a linear ordinary differential equation. The cases in question are depicted in Fig. 9a for the linearly increasing thermal profile and Fig. 9b for the linearly decreasing counterpart. In these instances, the effects of temperature inhomogeneity may be clearly seen in the shifting of the locus of the pressure peaks either upstream, toward the inlet of the tube, for the linearly increasing temperature profile, or downstream, toward the outlet, for the linearly decreasing $\tilde{T}_0(\tilde{x})$. Here too, the final locus of the stationary pressure antinodes becomes apparent after a full cycle. Similar observations obtained by Sujith et al. [79] lend support to the validity of the underlying framework.

2. Effects of Exponential and Harmonic Temperature Distributions

The exponentially varying temperature profile may be expressed in the form of $\tilde{T}_0(\tilde{x}) = k_0 e^{k_1 \tilde{x}}$, where k_0 and k_1 are yet to be determined. For an exponentially increasing temperature, one may impose $\tilde{T}_0(0) = 1$ and $\tilde{T}_0(1) = \alpha_e$, where α_e represents the spatial growth factor. In this case, one finds $k_0 = 1$ and $k_1 = \ln \alpha_e = \ln 2$ for a unit gain in temperature. Conversely, for the exponentially decreasing pattern, one may set $\tilde{T}_0(0) = \alpha_e$ and $\tilde{T}_0(1) = 1$. One deduces $k_0 = \alpha_e = 2$, and $k_1 = \ln(1/\alpha_e) = -\ln 2$ for a unit decrease in temperature. The resulting pressure predictions are provided in Fig. 10a for the exponentially growing profile and Fig. 10b for the exponentially decaying pattern. Graphically, the spatial variations of the pressure mode shapes may be seen to resemble their counterparts for the linearly varying temperature distributions; this behavior may be attributed to their comparable average values over the \tilde{x} -domain.

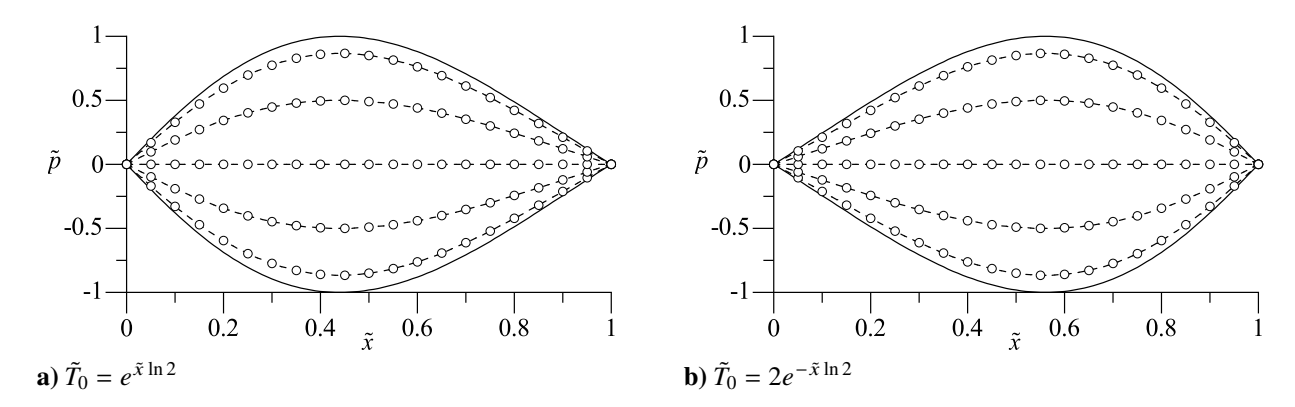


Fig. 10. Acoustic pressure variations corresponding to (a) exponentially increasing and (b) exponentially decreasing mean temperature profiles.

Along similar lines, sinusoidal temperature distributions can be examined with either harmonically increasing or decreasing thermal patterns. To ensure that the minimum non-dimensional temperature does not drop below unity, these are expressed as $\tilde{T}_0(\tilde{x}) = 1 + \sin(\pi \tilde{x}/2)$ and $\tilde{T}_0(\tilde{x}) = 1 + \cos(\pi \tilde{x}/2)$, and then shown in Figs. 11a and 11b, respectively. Furthermore, to investigate the effect of a complete thermal oscillation, the spatial distributions $\tilde{T}_0(\tilde{x}) = 1 + \sin(\pi \tilde{x})$ and $\tilde{T}_0(\tilde{x}) = 2 - \sin(\pi \tilde{x})$, which are also depicted in Figs. 11c and 11d, are considered. In comparison to the linear and exponentially varying patterns, the harmonic profiles exhibit the smallest deviations from the classic mode shapes. Overall, the nodal location and frequency vary slightly as one alternates from the exponentially increasing to the harmonically increasing cases. This upward shift may be attributed to the higher average temperature associated with the harmonically increasing profile. This increased temperature also modifies the structure of the outer mode shape envelope, which appears to swell for a harmonically increasing profile relative to Fig. 8a, and to shrink for a harmonically decreasing case. The attendant swelling and shrinkage in Fig. 11 become particularly noticeable near the endwalls.

In hindsight, the loci of the maximum acoustic pressure for the last two harmonic profiles in Figs. 11c and 11d do not change relative to a uniform temperature distribution because these profiles reflect symmetrically with respect to the chamber's midpoint. In fact, for all cases considered, the effect of a thermal variation may be evaluated relative to the benchmark case with no temperature gradient in Fig. 8a. For a profile exhibiting a higher temperature near a boundary, say $\tilde{x}=1$, the corresponding increase in the local speed of sound leads to a shift in the peak pressure away from that boundary, as experienced in Figs. 9a, 10a and 11a. Conversely, when the temperature decreases near a boundary, the locally reduced propagation speed leads to a shift in the peak pressure toward that boundary itself, and this shift is accompanied by an increased local pressure amplitude, namely, where the local speed of sound is reduced. This behavior is showcased in Figs. 9b, 10b and 11b.

3. Effects of Piecewise Temperature Distributions

When a heat source is present, zone-specific temperature profiles can be combined in a manner that is consistent with practical assumptions that are routinely made in the modeling of the thermal distribution in a Rijke tube. Two cases will be considered here and these consist of a constant-constant profile with a sudden jump at the heat source, and a constant-decaying exponential function that transitions at the heat source. In the first case, one may assume a uniform cold temperature followed by a uniform hot temperature with a jump discontinuity over the heater location at $\tilde{x} = 0.25$ [53]. The corresponding piecewise distribution may be written as

$$\tilde{T}_0(\tilde{x}) = \begin{cases} 1; & 0 \le \tilde{x} < \frac{1}{4} \\ k_0; & \frac{1}{4} \le \tilde{x} < 1 \end{cases}$$
(44)

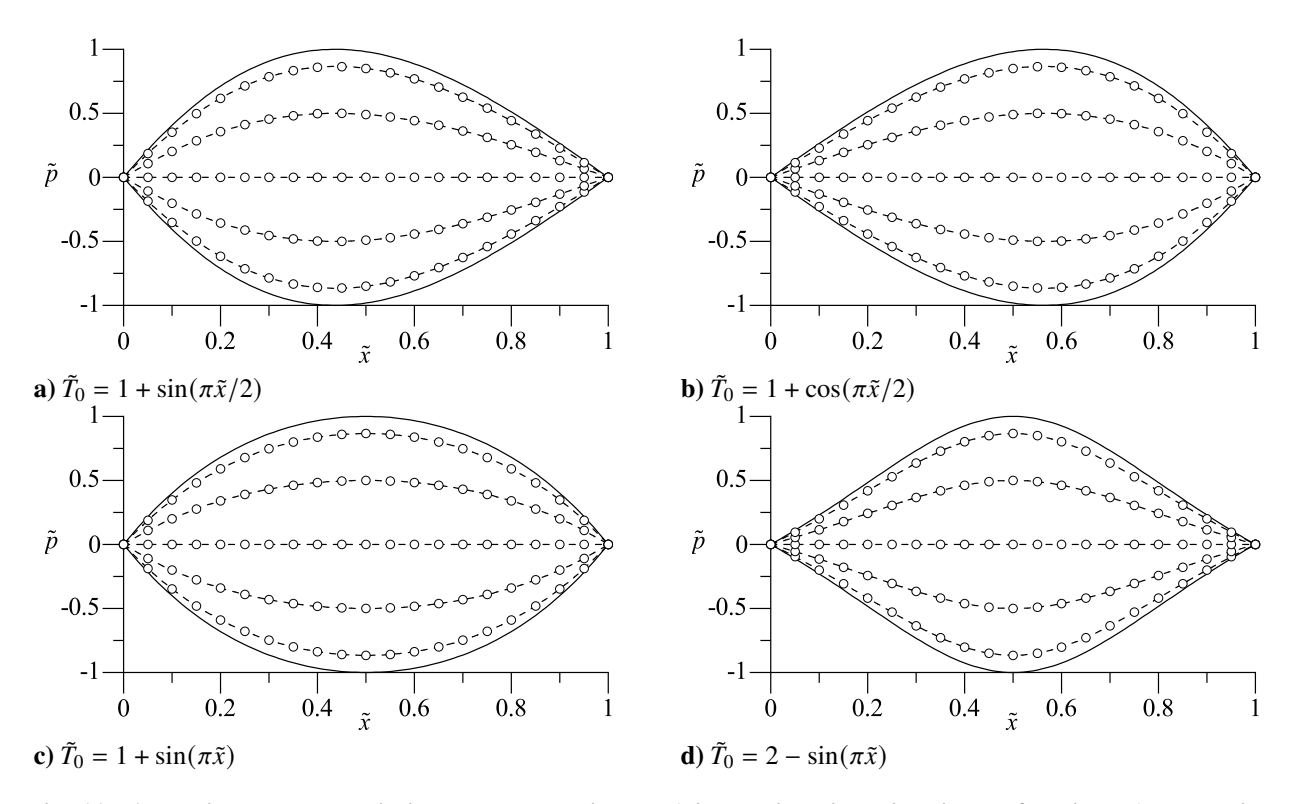


Fig. 11. Acoustic pressure variations corresponding to a) increasing sinusoid with half period, b) decreasing sinusoid with half period, c) increasing sinusoid, and d) decreasing sinusoid.

In the second model, a constant temperature may be assumed leading up to the heater, and this may be then followed by a smoothly decaying exponential function such as

$$\tilde{T}_0(\tilde{x}) = \begin{cases} 1; & 0 \le \tilde{x} < \frac{1}{4} \\ k_0 e^{k_1 \left(\tilde{x} - \frac{1}{4}\right)}; & \frac{1}{4} \le \tilde{x} < 1 \end{cases}$$
 (45)

In the above, k_0 represents the mean temperature at the heater location, and k_1 may be chosen in a manner to secure the outlet temperature at $\tilde{x} = 1$. Presently, we let $k_0 = 13/6$, and $k_1 = -1/5$ to be consistent with the experimental configuration described above. Specifically, these constants may be readily determined from the gain (650/300) and decay rate of the mean temperature time history computed for the present configuration [7].

Forthwith, the fluctuating pressure approximations for the two modeled Rijke temperature distributions are readily evaluated from Eq. (43) and provided in Figs. 12a and 12b. Firstly, the resulting approximations seem to corroborate the experimental findings of Kosztin et al. [91]; these suggest that deviations between constant-constant and constant-exponential temperature distributions may be neglected insofar as the pressure waveforms are concerned. In this vein, the constant-constant model's waveforms in parts **a**) and **c**) for the first two oscillation modes may be seen to exhibit a striking resemblance to their counterparts in parts **b**) and **d**) that are replicated using the constant-exponential thermal model.

Moreover, both models exhibit cusps at x = L/4 that are caused by the localized temperature discontinuities; unsurprisingly, these cusps diminish further downstream. A similar cusp formation is reported by Kosztin et al. [91], where it is corroborated by experiments and an analytical model for a quarter-length resonator. It is interesting to note that, in some models, a constant pressure amplitude is assumed across the heater element, which dismisses the possible presence of a sharp discontinuity. The pressure cusp that is captured here seems to indicate a steep pressure front at the heater location, a behavior that is consistent with the findings of Kosztin et al. [91] and Biwa et al. [68].

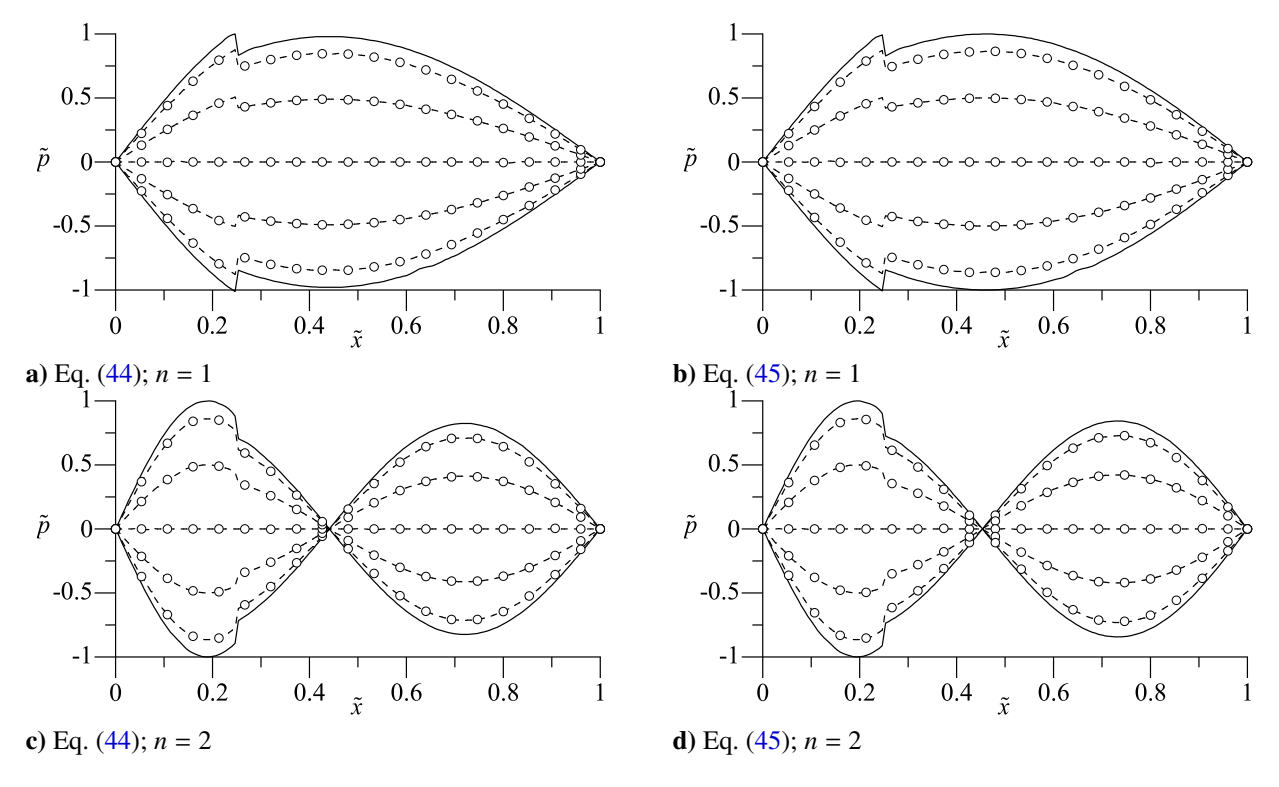


Fig. 12. Acoustic pressure variations corresponding to a) constant-constant and b) constant-decaying exponential mean temperature profiles for the first oscillation mode and, respectively, in c) and d) for the second oscillation mode. The jump in temperature occurs at the L/4 location.

Table 3. Comparison of predicted eigenvalues $(\tilde{\omega}_n^2)$ and corresponding non-dimensional circular frequencies with those of a numerical eigensolver [93].

Eigenvalue index	Analytical $\tilde{\omega}_n^2$	Numerical $\tilde{\omega}_n^2$	Analytical $\tilde{\omega}_n$	Numerical $\tilde{\omega}_n$	Relative error
1	14.381	14.338	3.792	3.787	0.00132
2	57.524	57.480	7.584	7.582	0.00026
3	129.430	129.386	11.378	11.375	0.00026
4	230.097	230.053	15.169	15.167	0.00013
5	359.523	359.483	18.961	18.960	0.00005
6	517.718	517.674	22.753	22.752	0.00004
7	704.672	704.628	26.546	26.545	0.00004
8	920.338	920.344	30.338	30.337	0.00003
9	1164.866	1164.822	34.130	34.130	0.00000
10	1438.108	1438.063	37.922	37.922	0.00000

4. Verification and Validation of Predicted Modal Frequencies

Having verified the spatial characteristics predicted by the asymptotic formulation, it is instructive to explore its temporal features. To do so, the frequencies associated with the eigenvalues of the resulting Sturm–Liouville problem may be evaluated and compared to predictions from other models. As such, the first fundamental frequency may be estimated to be

$$\tilde{f}_1 = \frac{\tilde{\omega}_1}{2\pi} = \frac{1}{2\Theta} \quad \text{and} \quad \tilde{\omega}_1 = \frac{\pi}{\Theta}$$
 (46)

The above expression displays a similar form to that used by Lieuwen [92]; it can be readily employed to predict higher harmonics with a sufficient degree of accuracy. In reverting back to dimensional variables, \tilde{f}_n may be simply multiplied by $(a_0)_{\min}/L$, where $(a_0)_{\min}$ stands for the lowest speed of sound in the tube, which is typically taken at the cold inlet; it is customarily taken to be approximately 347 m/s in most applications [50].

To illustrate the accuracy of the present approximation, the eigenvalues obtained based on the asymptotic expression, $\tilde{\omega}_n$, will be compared to a numerically evaluated Sturm-Liouville problem, using the program "Matslise" by Ledoux and Van Daele [93]. As shown in Table 3, we start by performing this comparison for the first ten eigenvalues using the same linear thermal profile, i.e., $\tilde{T}_0(\tilde{x}) = 1 + \tilde{x}$.

It is clear from Table 3 that the analytically calculated eigenvalues, which are based on an asymptotic formulation that is expected to increase in precision with successive increases in the mode number, remain quite accurate even at the lowest five modes. In fact, their relative deviations from their "true" values rapidly drop from 0.13% for the first fundamental frequency to 0.005% for the fifth mode. This accelerated convergence suggests that even though the asymptotic approximation only becomes "exact" at very large values of n, its predictions are still precise for the first few eigenmodes. On this note, and to further illustrate the accuracy of this spatially averaged frequency, we may proceed to compare predictions based on the ensuing asymptotic formulation to that developed by Sujith et al. [79].

Based on a well-recognized framework by Sujith et al. [79], the solution may be assumed to possess periodic time dependence to the extent of transforming it from a partial differential wave equation to an ordinary differential equation for the pressure mode shape. Algebraically, one gets,

$$\frac{\mathrm{d}^2 P'_n}{\mathrm{d}x^2} + \frac{1}{T_0} \frac{\mathrm{d}T_0}{\mathrm{d}x} \frac{\mathrm{d}P'_n}{\mathrm{d}x} + \frac{(2\pi f_n)^2}{\gamma R T_0} P'_n = 0,\tag{47}$$

where P'_n represents the *n*th pressure mode shape and the other variables retain their usual meaning. Since Eq. (47) cannot be solved directly for an arbitrary thermal profile, it may be conveniently transformed from the *x*-space to the

Table 4. Comparison of predicted frequencies with those of Sujith et al. [79] for various initial temperatures.

T_i [K]	Frequency [Hz] from Sujith et al. [79]	Frequency [Hz] from Eq. (46)	Relative deviation
500	49.67	49.71	0.0008
700	54.72	54.84	0.002
900	59.06	59.28	0.004
1100	62.92	63.25	0.005
3000	88.91	90.31	0.004

 T_0 -space using

$$\left(\frac{dT_0}{dx}\right)^2 \frac{d^2 P_n'}{dT_0^2} + \frac{1}{T_0} \frac{d}{dx} \left(T_0 \frac{dT_0}{dx}\right) \frac{dP_n'}{dT_0} + \frac{(2\pi f_n)^2}{\gamma R} \frac{P_n'}{T_0} = 0.$$
(48)

By completing this transformation, an exact solution may be retrieved for a user-specified temperature profile; however, solutions remain limited in scope as only a few profiles can be solved in conjunction with Eq. (48) [79, 82, 83]. In what follows, we present the solution corresponding to a linear thermal profile; an exponential profile can also be accommodated using the same procedure. A linear temperature profile enables us to rewrite Eq. (48) in such a manner to produce an exact solution in terms of zeroth-order Bessel functions. The corresponding dimensional pressure oscillation may be expressed as

$$P'_{n} = c_{1}J_{0} \left[\frac{2\pi f_{n}}{b} \sqrt{T_{0}(x)} \right] + c_{2}Y_{0} \left[\frac{2\pi f_{n}}{b} \sqrt{T_{0}(x)} \right]; \quad b \equiv \frac{|\alpha_{l}|}{2} \sqrt{\gamma R}.$$
 (49)

In the above, c_1 and c_2 denote two arbitrary constants, J_0 and Y_0 allude to the zeroth-order Bessel and Neumann functions, and α_l captures the temperature gain that controls the temperature gradient; presently, it represents the constant slope of the temperature in the tube; as for f_n , γ , and R, they allude to the Hertzian frequency of the nth mode, ratio of specific heats, and universal gas constant, respectively. To determine the frequency, one may impose boundary conditions that are appropriate for an open-open tube configuration, namely, where the pressure amplitude vanishes at both ends. Then, since the resulting algebraic equations prove to be homogeneous, one can suppress their determinant. The eigenfrequencies become those that will satisfy,

$$J_0 \left[\frac{2\pi f_n}{b} \sqrt{T_0(0)} \right] Y_0 \left[\frac{2\pi f_n}{b} \sqrt{T_0(L)} \right] - J_0 \left[\frac{2\pi f_n}{b} \sqrt{T_0(L)} \right] Y_0 \left[\frac{2\pi f_n}{b} \sqrt{T_0(0)} \right] = 0.$$
 (50)

For the sake of comparison, the test conditions described in Table 1 of Sujith et al. [79] are considered; however, conditions pertaining to an open-open tube configuration are imposed here, as opposed to the closed-open duct configuration that is closely examined by Sujith et al. [79]. Note that all cases employ a linearly decreasing profile with an arbitrary inlet temperature T_i and a fixed outlet temperature $T_o = 300 \text{ K}$ at x = L. Interestingly, the predicted duct frequency remains unaffected by whether the thermal profile is strictly increasing or decreasing: both cases lead to the same average frequency owing to their globally symmetric profiles and mean temperature values over the length of the tube. Nonetheless, reversing the temperature distribution does affect the pressure waveform, which becomes perfectly mirrored with respect to the tube's midpoint. This behavior may be partly attributed to the open-open tube configuration, namely, where an increasing temperature profile from the tube's inlet produces a similar effect on the mode shape to that of a similarly decreasing thermal profile from the outlet.

As one may infer from Table 4, a compelling agreement may be seen to exist between the frequencies deduced from the closed-form formulation given by Eq. (46) and those predicted from the well-established model by Sujith et al. [79]. Specifically, their relative differences vary from 0.08% for a modest thermal gradient with $T_i = 500$ K to 0.4% for a much steeper gradient with $T_i = 3000$ K. In all cases considered, Eq. (46) returns a very reasonable and straightforward prediction. Not only do we obtain a favorable frequency comparison, but, also, the corresponding acoustic mode shapes are found to be imperceptible. These are shown in Fig. 13 and Fig. 14, where the hollow circles associated with the model by Sujith et al. [79] are found to be rather indiscernible over the entire domain from the full and broken lines associated with the present formulation for the first and second oscillation modes. This excellent agreement may be attributed to the maximum discrepancy separating the two models at each time step being of $O(10^{-4})$; since such deviations are likely due to inevitable round-off errors, we can proceed to compare the asymptotic model's predictions using a more realistic thermal profile.

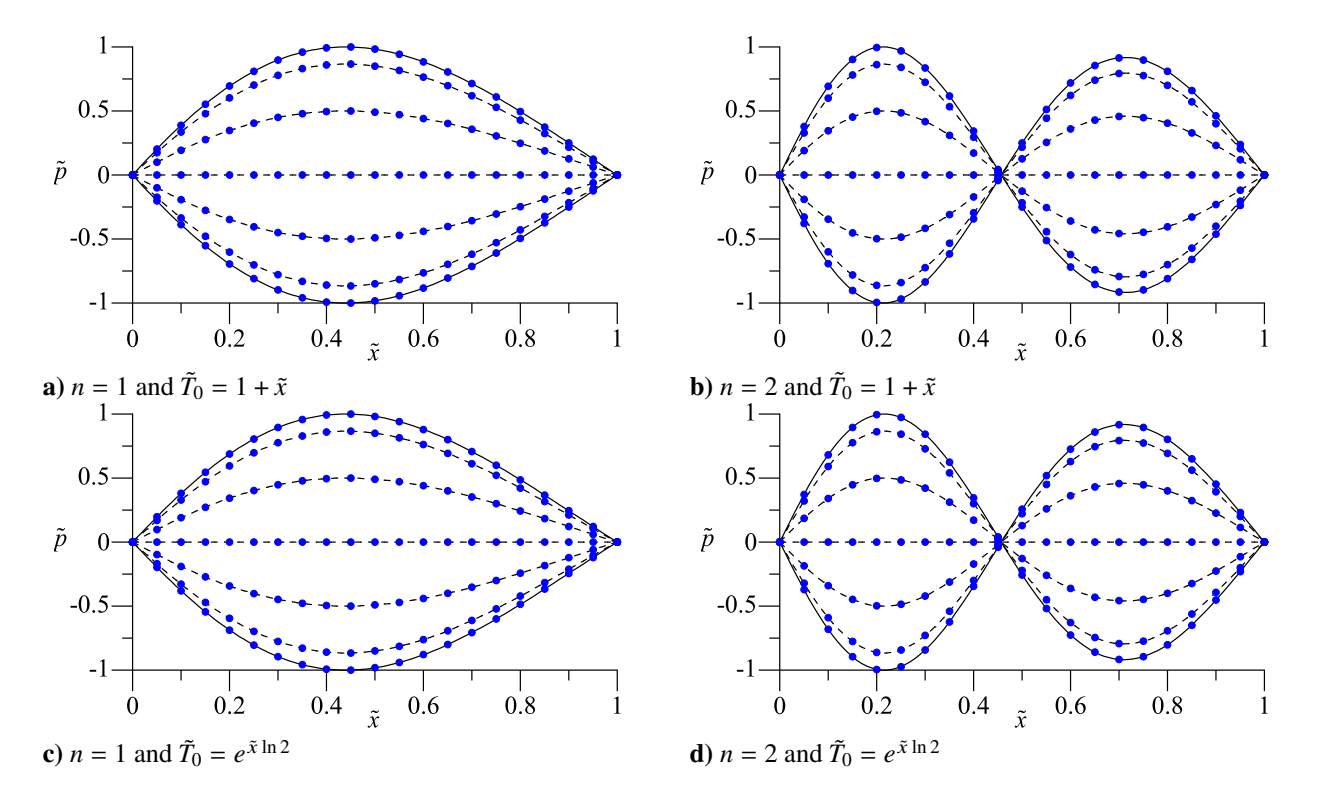


Fig. 13. Comparison between the acoustic pressure mode shape formulation based on Sujith et al. [79] using solid circles (\bullet) and the present asymptotic solution using both full lines (——) for the mode shape envelope and broken lines (---) for the remaining time history, taken every one-twelfth of a period. Both first and second oscillation mode shapes are illustrated successively in parts a) and b) for a linearly increasing function, $\tilde{T}_0(\tilde{x}) = 1 + \tilde{x}$, and in parts c) and d) for an exponentially increasing function, $\tilde{T}_0(\tilde{x}) = e^{\tilde{x} \ln 2}$.

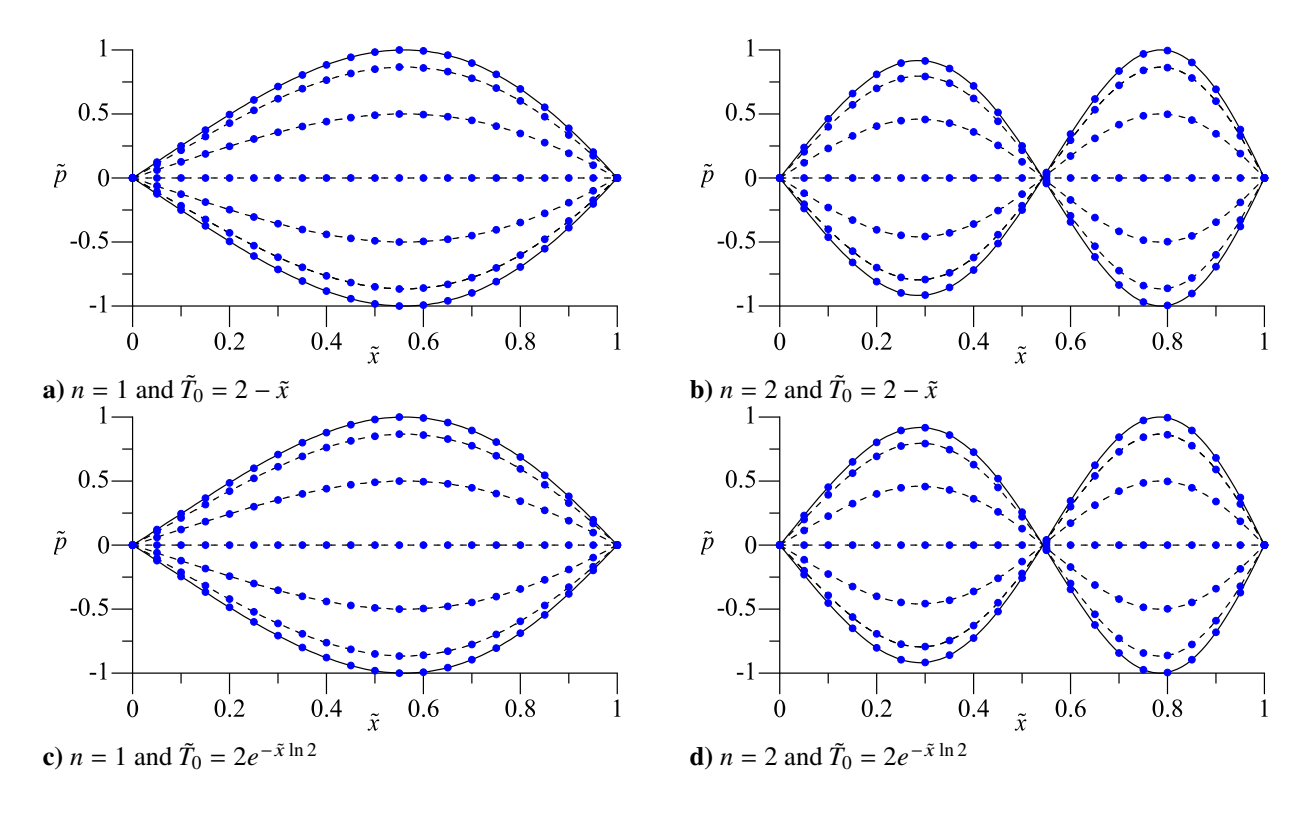


Fig. 14. Comparison between the acoustic pressure mode shape formulation based on Sujith et al. [79] using solid circles (\bullet) and the present asymptotic solution using both full lines (——) for the mode shape envelope and broken lines (---) for the remaining time history, taken every one-twelfth of a period. Both first and second oscillation mode shapes are illustrated successively in parts a) and b) for a linearly decreasing function, $\tilde{T}_0(\tilde{x}) = 2 - \tilde{x}$, and in parts c) and d) for an exponentially decreasing function, $\tilde{T}_0(\tilde{x}) = 2e^{-\tilde{x} \ln 2}$.

Table 5. Predicted frequency comparison for the actual Rijke tube.

Model	Predicted frequency [Hz]	Relative deviation
Green's function formulation by Bigongiari and Heckl [53]	246.5	0.006
Integral formulation by Lieuwen [92]	228.6	0.078
Constant-constant temperature profile given by Eq. (44)	253.9	0.023
Constant-exponential temperature profile given by Eq. (45)	247.6	0.001

Having verified the frequency formulation, the present model can be further vetted by comparing its predictions of the actual Rijke tube frequency to the distinct models developed by Bigongiari and Heckl [53] as well as Lieuwen [92]. As shown in Table 5, this may be accomplished using both the constant-constant and constant-decaying exponential temperature profiles defined through Eqs. (44) and (45), respectively. The underlying test case is chosen to be the temperature distribution obtained from the experimental results discussed in Sec. VI.A. At the outset, we recall that the most reliable experimental measurement given in Table 1 corresponds to a frequency of $f_{\text{exp}} = 248 \,\text{Hz}$ for a microphone placement that is adjacent to the heater element; this value will be treated as the true frequency in the tube.

In the first case, using a constant-constant temperature profile, the one-term integral method based on Eqs. (44) and (46) yields a dimensional frequency of 253.9 Hz, which is only 2.3% higher than $f_{\rm exp}$. Using the method developed by Lieuwen [92], a frequency of 228.6 Hz is retrieved, with a deviation of 7.8%. The method devised by Bigongiari and Heckl [53] returns a frequency of 246.5 Hz, which undershoots the experimental value by a mere 0.6%. The accuracy of the constant-constant temperature profile with a jump discontinuity supports the statement made by Kosztin et al. [91] on the validity of assuming a constant temperature within a tube above and below the heater element. Clearly, the assignment of uniform temperatures to the hot and cold segments of the Rijke tube leads to reasonable results.

In the second case, a realistic constant-exponential temperature profile is used; we recall that this particular model is based on the two-parameter thermal distribution that is guided by numerical simulations of the actual experimental configuration and leading to Eq. (45). In this case, our asymptotic approximation, given by Eq. (46), produces a frequency of 247.6 Hz, thus entailing a negligible deviation of 0.1%; since the latter falls well within experimental uncertainty, the predicted frequency may be viewed as being essentially identical to $f_{\rm exp}$. Moreover, the evaluation of Eq. (46) remains straightforward, requiring the least intensive computations and excluding a flame describing function specification. In fact, the ability to predict the frequency directly from the temperature profile gives further credence to the asymptotic framework at leading order. As for the unsteady heat release oscillations, they may be deferred to higher asymptotic orders.

5. Locus of Acoustic Pressure Peaks

So far, it has been well established that temperature gradients not only affect the frequency and mode shapes, but also the locus of the maximum pressure antinode. The latter represents a fundamental property of a thermoacoustic system that will be useful to characterize especially that it directly alters the structure of the standing waveform. To pinpoint the corresponding antinodes, one may start with the pressure eigenfunction, given by Eq. (41), which prescribes the spatial mode shape pattern. The locus of the temperature-sensitive pressure peaks may then be determined by suppressing the derivative of the eigenfunction while setting

$$\frac{\mathrm{d}}{\mathrm{d}\tilde{x}} \left[\frac{y_n(\tilde{x})}{\|y_n\|} \right] = \frac{4n\pi}{\Theta} \sqrt{\tilde{T}_0(\tilde{x})} \cos \left[\frac{n\pi}{\Theta} \int_0^{\tilde{x}} \frac{1}{\sqrt{\tilde{T}_0(\tilde{x})}} \, \mathrm{d}\tilde{x} \right] - \frac{\mathrm{d}\tilde{T}_0(\tilde{x})}{\mathrm{d}\tilde{x}} \sin \left[\frac{n\pi}{\Theta} \int_0^{\tilde{x}} \frac{1}{\sqrt{\tilde{T}_0(\tilde{x})}} \, \mathrm{d}\tilde{x} \right] = 0. \tag{51}$$

In the interest of brevity, the focus will be on the behavior for n = 1; we get:

$$\frac{\mathrm{d}}{\mathrm{d}\tilde{x}} \left[\frac{y_1(\tilde{x})}{\|y_1\|} \right] = \frac{4\pi}{\Theta} \sqrt{\tilde{T}_0(\tilde{x})} \cos \left[\frac{\pi}{\Theta} \int_0^{\tilde{x}} \frac{1}{\sqrt{\tilde{T}_0(\tilde{x})}} \, \mathrm{d}\tilde{x} \right] - \frac{\mathrm{d}\tilde{T}_0(\tilde{x})}{\mathrm{d}\tilde{x}} \sin \left[\frac{\pi}{\Theta} \int_0^{\tilde{x}} \frac{1}{\sqrt{\tilde{T}_0(\tilde{x})}} \, \mathrm{d}\tilde{x} \right] = 0. \tag{52}$$

This relation may be solved asymptotically or using a root finding program to determine the location of the pressure antinodes for any given $\tilde{T}_0(\tilde{x})$. For the simple case of a uniform profile, the maximum pressure location, \tilde{x}_{max} , may be readily identified. Noting that the axial temperature derivative vanishes for $\tilde{T}_0 = 1$, one is left with,

$$\cos\left(\pi\tilde{x}_{\text{max}}/\Theta\right) = 0. \tag{53}$$

Table 6. Non-dimensional acoustic pressure peak locations based on various thermal profiles exhibiting either zero or unitary temperature variations.

$\tilde{T}_0(\tilde{x})$	Θ	$\tilde{\omega}_1 = \pi/\Theta$	\tilde{x}_{\max}
$\tilde{T}_0(\tilde{x}) = 1$	1	$\pi \approx 3.14159$	0.50000000
$\tilde{T}_0(\tilde{x}) = 1 + \tilde{x}$	$2(\sqrt{2}-1)\approx 0.828427$	$\pi/[2(\sqrt{2}-1)] \approx 3.79224$	0.43968790
$\tilde{T}_0(\tilde{x}) = 2 - \tilde{x}$	$2(\sqrt{2}-1)\approx 0.828427$	$\pi/[2(\sqrt{2}-1)] \approx 3.79224$	0.56031210
$\tilde{T}_0(\tilde{x}) = 1 + \tilde{x}^2$	$\ln(1+\sqrt{2}) \approx 0.881374$	$\pi/\ln(1+\sqrt{2})\approx 3.56443$	0.43782274
$\tilde{T}_0(\tilde{x}) = e^{\tilde{x} \ln 2}$	$(2-\sqrt{2})/\ln 2 \approx 0.845111$	$\pi \ln 2/(2-\sqrt{2}) \approx 3.71737$	0.43984995
$\tilde{T}_0(\tilde{x}) = 2e^{-\tilde{x}\ln 2}$	$(2-\sqrt{2})/\ln 2 \approx 0.845111$	$\pi \ln 2/(2-\sqrt{2}) \approx 3.71737$	0.56015005
$\tilde{T}_0(\tilde{x}) = 1 + \sin(\pi \tilde{x}/2)$	$(\sqrt{2}/\pi) \ln(3 + 2\sqrt{2}) \approx 0.793515$	$\pi^2/[\sqrt{2}\ln(3+2\sqrt{2})] \approx 3.95908$	0.43679651
$\tilde{T}_0(\tilde{x}) = 1 + \cos(\pi \tilde{x}/2)$	$(\sqrt{2}/\pi) \ln(3 + 2\sqrt{2}) \approx 0.793515$	$\pi^2/[\sqrt{2}\ln(3+2\sqrt{2})] \approx 3.95908$	0.56320349
$\tilde{T}_0(\tilde{x}) = 1 + \sin(\pi \tilde{x})$	$(\sqrt{2}/\pi)\ln(3+2\sqrt{2})\approx 0.793515$	$\pi^2/[\sqrt{2}\ln(3+2\sqrt{2})] \approx 3.95908$	0.50000000
$\tilde{T}_0(\tilde{x}) = 2 - \sin(\pi \tilde{x})$	$\left \frac{4}{\pi} \text{EllipticF} \left(\frac{1}{4} \pi \right) - 2 \right) \approx 0.872278$	$\pi^2/\left[4 \text{ EllipticF}\left(\frac{1}{4}\pi\right -2\right)\right] \approx 3.60159$	0.50000000

As expected, one quickly recovers $\Theta=1$ and $\tilde{x}_{max}=0.5$. Along similar lines, the loci of the nine other non-uniform temperature profiles may be computed and cataloged one-by-one in Table 6. We note on this occasion that despite their dissimilar forms, the spatially varying profiles lead to the same unitary temperature variation across the solution domain, as illustrated in Fig. 7. For this reason, the corresponding shifts in pressure peaks prove to be comparable in value and dependent on the sign of the temperature gradient.

More specifically, for a monotonically decreasing temperature over the entire domain, the antinode will shift toward the aft end of the tube. Conversely, for a monotonically increasing temperature, the antinode will slide forward. A steeper gradient seems to perturb the nodal location the most, as it leads to a relatively larger disparity in the local speed of sound. This is corroborated by the case of a half sinusoid, where the nodal location shifts toward the inlet by 12.6%, notwithstanding the modest unitary temperature gain. From this limited group of test functions, the quadratic profile produces the second largest peak pressure shift of 12.4%. Interestingly, for thermal profiles exhibiting reflective symmetry with respect to the midsection plane, their antinodes remain stationary (e.g., the uniform and full sinusoidal functions). In these instances, the left and right traveling waves, which reflect off the endpoints, will propagate at the same average speeds after crossing regions with symmetrical thermal distributions. At the outset, their consolidated maximum amplitudes will remain anchored at the tube's midpoint. As for the antisymmetric profiles, such as the increasing or decreasing linear, exponential, and half sinusoidal functions, their antinodes remain equidistant from the midpoint location; their \tilde{x}_{max} values can be shown to be strictly complementary, always adding up to unity.

Besides numerically calculating the peak pressure locations, it is possible to manipulate their defining equations asymptotically. For example, Eq. (52) may be rearranged into

$$\frac{\mathrm{d}\tilde{T}_0(\tilde{x})}{\mathrm{d}\tilde{x}}\tan\left[\frac{\pi}{\Theta}\int_0^{\tilde{x}}\frac{1}{\sqrt{\tilde{T}_0(\tilde{x})}}\,\mathrm{d}\tilde{x}\right] - \frac{4\pi}{\Theta}\sqrt{\tilde{T}_0(\tilde{x})} = 0. \tag{54}$$

In principle, Eq. (54) can be expanded algebraically and then solved for any temperature distribution, including one that contains an arbitrary thermal gain, $\tilde{\alpha}$. For the sake of illustration, four test functions will be considered, namely, the conventional linear and exponential thermal profiles with increasing and decreasing gradients. These may be written as

$$\tilde{T}_{0} = \begin{cases} 1 + \tilde{\alpha}_{l}\tilde{x} & \text{(linear increase)} & \text{or} \quad 1 + \tilde{\alpha}_{l}(1 - \tilde{x}) & \text{(linear decrease),} \\ e^{\tilde{x}\ln(\tilde{\alpha}_{e}+1)} & \text{(exponential growth)} & \text{or} \quad (\tilde{\alpha}_{e}+1)e^{-\tilde{x}\ln(\tilde{\alpha}_{e}+1)} & \text{(exponential decay),} \end{cases}$$
(55)

where $\tilde{\alpha}_l$ and $\tilde{\alpha}_e$ prescribe the non-dimensional slopes and growth rate coefficients of the linear and exponential profiles, respectively. These coefficients control the temperature gradients across the domain and are selected such that setting $\tilde{\alpha}_l = \tilde{\alpha}_e = 0$ restores the case of a uniform thermal profile with $\tilde{x}_{max} = 0.5$. In fact, the temperature range in all four cases remains strictly equal to $\tilde{\alpha}$, being bracketed between unity and $1 + \tilde{\alpha}$ for $\tilde{x} \in [0, 1]$.

For modest temperature gradients, it is convenient to solve Eq. (54) by extracting the small deviation from the traditional antinodal location at $\tilde{x}_{max} = 0.5$. Inspired by the entries in Table 6, one may express the pressure antinode

in terms of a small correction, $\tilde{\epsilon} \leq 0.25$, specifically,

$$\tilde{x}_{\text{max}} = \begin{cases}
0.5 - \tilde{\epsilon} & (\text{for } \nabla T_0 > 0 \text{ and } \tilde{\alpha} \leq \tilde{\alpha}_{\text{lim}}) & \text{or } \tilde{\epsilon} & (\text{for } \nabla T_0 > 0 \text{ and } \tilde{\alpha} > \tilde{\alpha}_{\text{lim}}), \\
0.5 + \tilde{\epsilon} & (\text{for } \nabla T_0 < 0 \text{ and } \tilde{\alpha} \leq \tilde{\alpha}_{\text{lim}}) & \text{or } 1 - \tilde{\epsilon} & (\text{for } \nabla T_0 < 0 \text{ and } \tilde{\alpha} > \tilde{\alpha}_{\text{lim}}),
\end{cases}$$
(56)

In practice, a large thermal gain corresponds to a value $\tilde{\alpha}_{lim}$ that causes the pressure peak to shift by more than a quarter distance from the tube's midpoint. Being dependent on the actual temperature profile, we find $\tilde{\alpha}_{lim} \approx 31.98$ and 35.86 for the linear and exponential distributions in Eq. (55), respectively.

At this stage, Eqs. (55) and (56) may be substituted back into Eq. (54) and then used to predict the dependence of \tilde{x}_{max} on $\tilde{\alpha}_l$ or $\tilde{\alpha}_e$, as shown in Fig. 15, for the four representative test functions. Therein, the peak acoustic pressure loci are depicted firstly in Figs. 15a and 15b using a logarithmic scale and a broad range of $\tilde{\alpha} \in [10^{-2}, 10^4]$ and, secondly in Figs. 15c and 15d, using a magnified inset over a linear scale and a practical range of $\tilde{\alpha} \in [0, 20]$. In all cases considered, full lines and broken lines are used to differentiate between the loci associated with increasing temperature profiles and those referring to their decreasing mirror functions.

Forthwith, several observations can be made based on these graphs. First, in view of the antisymmetric character of each of the linear and exponential profiles, one may confirm the symmetrical displacement of the loci above and below the tube's midpoint for any fixed value of the temperature gain. As such, the sum of any two loci for a given $\tilde{\alpha}$ will equate to unity. Second, despite the large disparity in the basis functions associated with the linear and exponential profiles, the curves defining their loci may be seen to bear a striking resemblance, especially in the practical range of thermal gains depicted in Figs. 15c and 15d; one may infer that the loci remain strongly dependent on the thermal gain itself, irrespective of the functional form used to describe the temperature distribution. This behavior is corroborated by the findings of Kosztin et al. [91]. Third, in the practical range of $\tilde{\alpha} \in [0, 20]$, the antinodal shift from the midpoint location does not exceed 0.228; this represents a 45.6% excursion for a gain of $\tilde{\alpha} = 20$. Fourth, the temperature gradient needed to effectuate a fixed deviation in the antinodal location becomes progressively larger with successive increases in $\tilde{\alpha}$. For example, using the linear growth distribution in Fig. 15a, the antinodal shift may be seen to decrease from $\tilde{x}_{max} \approx 0.31028$ to 0.20737, 0.16955, and 0.16649 as $\tilde{\alpha}_l$ is increased from 10 to 10^2 , 10^3 , and 10^4 . The ensuing variation in \tilde{x}_{max} diminishes from 33.2% to 18.2% and 1.80% with each order-of-magnitude gain increment. Due to this asymptotic plateauing, it becomes virtually infeasible to modify the antinodal location by any appreciable amount without requiring an impractically large temperature gain.

Before leaving this subject, it may be instructive to illustrate the mode shape patterns associated with a thermal profile with a relatively steep gradient. Using a characteristic gain of $\tilde{\alpha}_e = 5$ in concert with an exponential function, acoustic pressure mode shapes corresponding to both steeply increasing and decreasing mean temperature profiles are generated and displayed in Fig. 16. These are shown in succession for the first and second oscillation mode numbers in Figs. 16a and 16b and, similarly, in Figs. 16c and 16d for the exponentially increasing and decreasing functions; the latter are given by $\tilde{T}_0 = e^{\tilde{x} \ln 6}$ and $\tilde{T}_0 = 6e^{-\tilde{x} \ln 6}$, respectively. As usual, the timelines are taken every one-twelfth of a period, thus leading to a precise overlap between equispaced lines sweeping over the first and second half cycles. For this particular thermal gain, the maximum acoustic pressure of the first fundamental standing waveforms may be seen to shift to $\tilde{x}_{\text{max}} \approx 0.3538$ in Fig. 16a and to its complementary value of 0.6462 in Fig. 16c. For the second oscillation mode, the dual loci per waveform yield $\tilde{x}_{\text{max}} \approx 0.1720$ and 0.6392 in Fig. 16b for the primary and secondary antinodes. Their complementary values in Fig. 16d are found to be 0.8280 and 0.3608, respectively. Here too, the sum of each set of complementary peak pressure loci returns a unit value. Being outside the original scope of this study, the characterization of antinodal pressure loci for higher oscillation modes and other thermal functions will be relegated to a later investigation.

Lastly, and as alluded to earlier, although the focus of this study has been centered on the determination of the pressure waveforms and frequencies, it is possible to formulate and evaluate the equations leading to the fluctuating velocity and heat oscillations directly from Eqs. (28) and (29) at successive orders in ε . It is also possible to obtain higher-order approximations of the pressure waveforms and frequencies based on the underlying framework. Through this endeavor, the Rijke tube's thermoacoustic instability behavior may be closely examined along with the influence of various temperature gradients and boundary conditions on the attendant mode shape coupling. To keep this work manageable, however, the development and further analysis of higher-order properties will be deferred to future work.

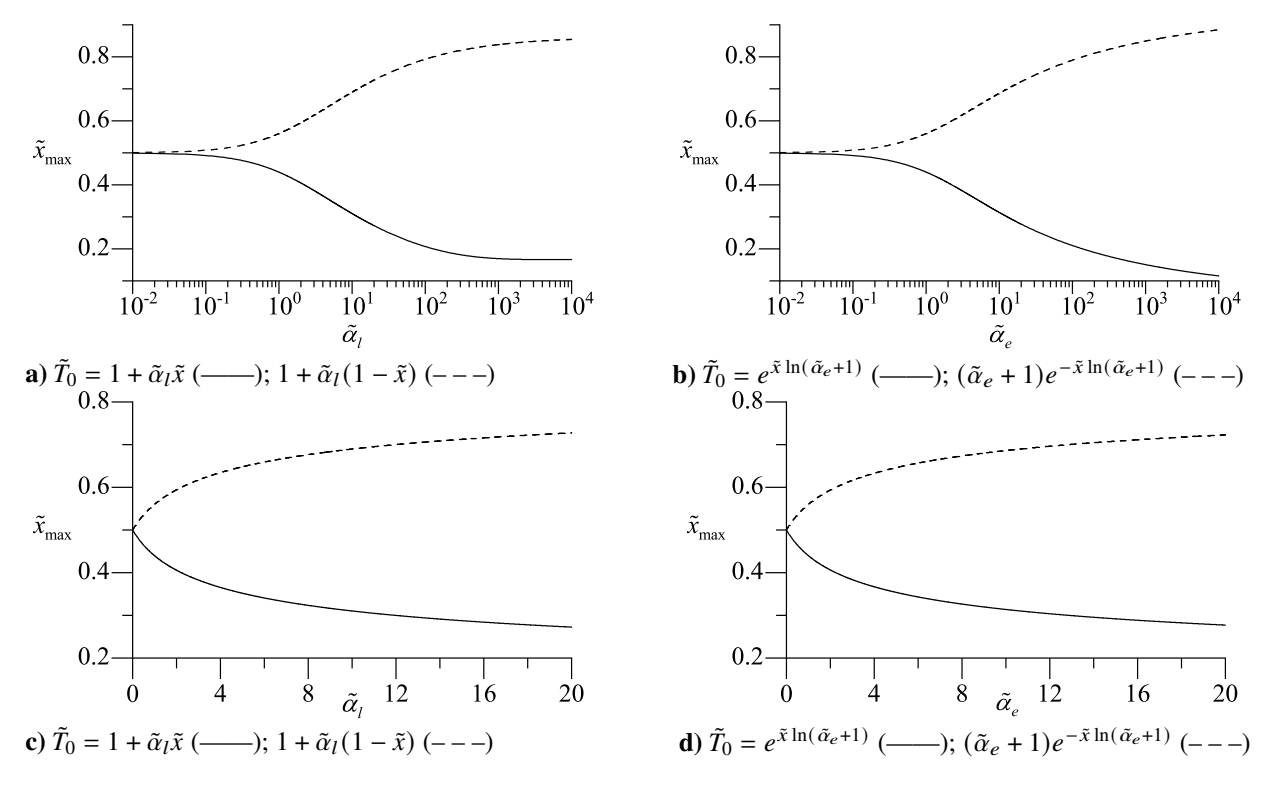


Fig. 15. Peak acoustic pressure loci as a function of the thermal gain for both a) linear and b) exponential temperature distributions using a logarithmic scale in $\tilde{\alpha} \in [10^{-2}, 10^4]$. Magnified insets are provided, respectively, in c) and d) using a linear scale and a practical range of $\tilde{\alpha} \in [0, 20]$. In all cases, full lines (——) and broken lines (——) denote the loci for increasing or decreasing temperature profiles, respectively.

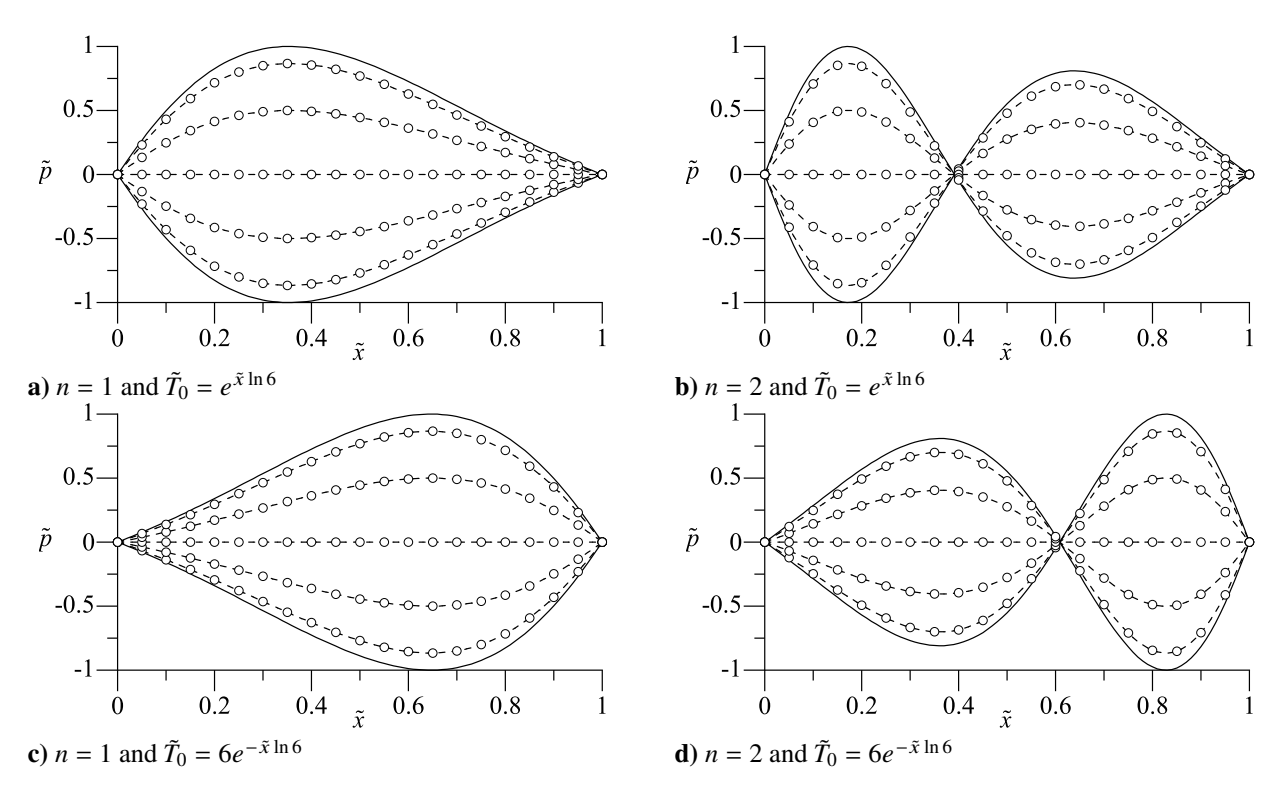


Fig. 16. Acoustic pressure variations corresponding to (a-b) steeply increasing and (c-d) decreasing mean temperature profiles using a characteristic gain of $\tilde{\alpha}_e = 5$. Both first and second oscillation mode shapes are illustrated successively in parts a) and b) for an exponentially growing function, $\tilde{T}_0 = e^{\tilde{x} \ln 6}$, and in parts c) and d) for an exponentially decaying function, $\tilde{T}_0 = 6e^{-\tilde{x} \ln 6}$. As usual, full lines (——) demarcate the mode shape envelope whereas broken lines (---) and hollow circles (\circ) represent evenly incremented timelines, taken every one-twelfth of a period, over the first and second half periods, respectively.

VIII. Summary

This work overviews six different perspectives on the prediction of acoustic pressure mode shapes and frequencies in a conventional Rijke tube resonator. The latter consists of a routinely invoked thermoacoustic energy conversion device which, when properly triggered with an unsteady heat source, can be used to showcase rather compellingly the application of Rayleigh's criterion.

At first, traditional experimental and computational approaches are undertaken partly to confirm the Rijke's sound generation capability and, partly, to generate benchmark data that can be used to gauge the accuracy of other theoretical models. This is followed by a scaling procedure that exposes fourteen non-dimensional parameters of which several may be relevant to thermoacoustic stability theory. By way of modeling the underlying equations of motion, two particularly innovative methods of analysis are examined. These include the pressure mode shape differential equation and the Green function techniques that have been judiciously spearheaded by Matveev [51] and Heckl [54], respectively. These are complemented by a simple asymptotic formulation that takes into account a naturally occurring small parameter that conveniently depends on the ratio of specific heats, namely, $\varepsilon = (\gamma - 1)/\gamma < 1$. The ensuing perturbative approach, when used in conjunction with a Green's function formulation, enables us to prescribe the acoustic pressure mode shape patterns and frequencies directly as a function of the mean temperature profile within the tube. It also permits the identification of the asymptotic order at which the actual heat oscillation characteristics affect the acoustic pressure and velocity. Although the asymptotic formulation can be carried out to an arbitrary order, the expansion approach is evaluated for the pressure at the leading order of the perturbation parameter, ε . In the interest of brevity, higher approximations are deferred to later work. Presently, the evaluation of this technique remains limited in scope to a dozen test cases and representative thermal profiles that help to demonstrate its versatility at resolving the acoustic pressure field. The method's unique features are also showcased through side-by-side comparisons of pressure mode shapes and frequency predictions to other available formulations such as those by Matveev [51], Heckl et al. [52–55], Lieuwen [92], and Sujith et al. [79].

In hindsight, the dimensional analysis may be viewed as being useful at identifying several similarity parameters, nine to be precise. In addition to the expected geometric scaling ratios, reduced temperature, and thermal expansion factor, these include the unsteady Reynolds, Eckert, Mach, Nusselt, Prandtl, Grashof, and Strouhal numbers, with the latter returning the longitudinal mode number. We also come across two additional parameters: the first, $k_0T'/(p'u'D)$, gauges the relative importance of unsteady heat conduction to the energy flux vector modulus. The second grouping corresponds to a thermoacoustic energy conversion factor consisting of the ratio of the fluctuating heat release and the energy flux vector modulus. It is given by

$$Rj = \frac{(q'/D^2)}{p'u'} (57)$$

Theoretically, this parameter represents a key characteristic of the acoustic motion in a Rijke tube and, possibly, other thermoacoustic devices incorporating flame dynamics. In Noiray et al. [76], it is shown that oscillations occur in different state-space trajectories in the presence of nonlinear thermoacoustic feedback. Therein, triggering occurs for the type of oscillations that are modulated by a similar non-dimensional parameter. In this work, the significance of this parameter is ascertained both numerically and experimentally.

In addition to the dimensional analysis, the experimental effort that we describe serves to provide an independent verification of the unsteady flow attributes. For example, one is able to confirm that proper positioning of the heat source is crucial for effective thermoacoustic coupling. When the heat source is moved to either pressure or acoustic nodes, no acoustic amplification may be observed. The same occurs when the acoustic velocity and pressure become out of phase at the heater location. Conversely, when the heat source is positioned at one-fourth the distance from the tube's inlet station, the sound emitted by the pressure waves is maximized. This optimal position corresponds to the peak product of acoustic pressure and velocity which, algebraically, translates into the largest energy-flux vector modulus, $||p'u'||_{\text{max}}$. When gravitating away from this particular station, a reduction in the acoustic amplitude is realized. The experimental investigation also confirms the role of the air's mean convection currents in promoting the coupling between acoustic variables. Practically, unless the air's mean flow is appreciable, no acoustic amplification can occur. In fact, when forced convection currents are induced using external means, such as air blowers or displacement fans, acoustic amplification may be achieved in any flow orientation, be it vertical, oblique, or horizontal. Forced air currents can thus compensate for the lack of buoyancy in a horizontal tube configuration. Unsurprisingly, we find that sealing the top section of the tube drastically alters the wave character to the extent of suppressing any chance for acoustic excitation when the heat source is placed at a quarter-distance from the inlet section.

In this investigation, the optimal position of the heat source is reaffirmed using both laboratory and numerical

experiments. Particularly, our observations suggest that i) a minimum heat input is needed to trigger acoustic growth, ii) a critical heat input can lead to resonance, iii) a 45° phase difference exists between the acoustic pressure and the fluctuating heat release, and iv) the maximum acoustic amplification occurs when the product of acoustic velocity and pressure is largest. These conclusions seem consistent with other observations made in the literature.

Following this three-pronged analysis of the Rijke tube's flowfield, two modern techniques are examined, and these are primarily due to Matveev [51] as well as Heckl [54]. On the one hand, Heckl's approach takes into perspective the notion that a Green's function, defined as the acoustic potential field generated by an impulsive point source, can be used to model the sudden heat source and thermal jump across a heater element [53]. Using a one-dimensional velocity potential formulation with a fluctuating heat release, this approach leads to an effective model for the fluctuating velocity at the heater location. Moreover, its solution captures the feedback loop between the fluctuating heat release and the acoustic velocity; this nonlinear feedback can serve to alter the eigenvalues' real Hertzian frequencies as well as their imaginary growth rate coefficients. In this work, we confirm that Heckl's predicted frequency tends to be quite precise, resulting in compelling agreement with Rijke tube measurements and computations.

On the other hand, Matveev[51] introduces the notion of complex mode shapes while transforming the pressure wave equation with various sources, such as the fluctuating heat release and boundary-layer losses, into an ordinary differential equation. By leveraging proper matching conditions around the heat source, his formulation is capable of correctly accounting for both the temperature gradient and the fluctuating heat release within the tube. In practice, his resulting equation can be iteratively solved using finite differences in concert with a shooting method that converges on the particular eigenfrequencies that satisfy the problem's imposed boundary conditions. Although Matveev's formulation is designed to handle a continuous temperature distribution along the Rijke tube, his approach is reconstructed here using a piecewise function. This is accomplished by specifying two distinct temperature zones above and below the heat source. In this manner, by dividing the solution domain into two segments with dissimilar thermal profiles, the iterative solution procedure is superseded by a strictly analytical formulation for the complex mode shapes and frequencies. Specifically, by leveraging the Green's function formulation pioneered in this context by Heckl and coworkers, one is able to retrieve accurate solutions for the pressure, velocity, and heat release. Here too, Matveev's reconstructed solution proves to be quite dependable when compared to numerical simulations.

Guided by the foregoing models, a new asymptotic formulation is developed and evaluated for several representative thermal profiles; these include uniform, linear, quadratic, exponential, and sinusoidal functions as well as constantconstant and constant-decaying exponential temperature distributions. This perturbation approach is shown to be quite effective at reproducing the acoustic pressure mode shapes, peak values, and frequencies for an arbitrary thermal profile, be it continuous or piecewise. Moreover, the perturbative analysis helps to identify the orders at which the specified temperature and heat release oscillations affect the pressure mode shapes. On the one hand, the mean flow temperature is found to occupy the most essential role in prescribing the acoustic pressure's modal structure. More specifically, the temperature gradient is found to be the most essential factor affecting the mode shape structure [91]. This includes the acoustic pressure's peak loci which appear to be mainly controlled by the thermal gain irrespective of the actual temperature distribution. The latter seems to have a greater impact on the frequency evaluation, which remains dependent on a spatial integration of the mean thermal profile. On the other hand, the same perturbation expansion shows that the fluctuating heat release plays a secondary role in the sense that its contribution appears at the first order in ε . Although the expansion approach remains linear and insufficient to predict limit-cycle amplitudes, its application is rather straightforward at successive orders. In fact, its simplicity helps to unravel the defining equations for the acoustic velocity and fluctuating heat release at successive orders. In this work, the perturbative approach is leveraged to derive the acoustic mode shapes, pressure peaks, and frequencies, albeit at leading order only. These are then validated and verified through comparisons to both experimental measurements and numerical estimates obtained from other available formulations.

In future work, we hope to refine and extend the perturbation model to higher asymptotic orders in a manner to resolve not only the acoustic pressure waveforms, but also those prescribing the velocity and heat release. We also hope to enhance its capabilities by incorporating the effects of diverse boundary conditions, a finite mean flow, complex frequencies, and viscous losses.

Acknowledgments. This work was supported partly by Sierra Space Corporation, through contract № G460817, and partly by the National Science Foundation, through grant № CMMI-1761675. The senior author is appreciative of the supplemental support received internally from Auburn University, Department of Aerospace Engineering, through the Hugh and Loeda Francis Chair of Excellence. Both authors are deeply indebted to Martin J. Chiaverini, Donald Benner, Brian Pomeroy, and Arthur Sauer, for numerous technical exchanges.

References

- [1] Carrier, G. F., "The Mechanics of Rijke Tube," *Quarterly of Applied Mathematics*, Vol. 12, No. 4, 1955, pp. 383–395. doi:10.1090/gam/69698.
- [2] Chu, B.-T., "Stability of Systems Containing a Heat Source The Rayleigh Criterion," Research Memorandum 56D27, 1956.
- [3] Miller, J. and Carvalho, J. A., "Comments on Rijke Tube," Scientific American, Vol. 204, No. 3, 1961, pp. 180–182.
- [4] Maling, G. C., "Simplified Analysis of the Rijke Phenomenon," *Journal of the Acoustical Society of America*, Vol. 35, 1963, pp. 1058–1060. doi:10.1121/1.1918658.
- [5] Zinn, B. T., "State of the Art Research Needs of Pulsating Combustion," Noise Control and Acoustics, Vol. 84-WA NCA-19, 1984.
- [6] Raun, R. L., Beckstead, M. W., Finlinson, J. C., and Brooks, K. P., "Review of Rijke Tubes, Rijke Burners and Related Devices," *Progress in Energy and Combustion Science*, Vol. 19, No. 4, 1993, pp. 313–364. doi:10.1016/0360-1285(93)90007-2.
- [7] Entezam, B., Van Moorhem, W. K., and Majdalani, J., "Two-Dimensional Numerical Verification of the Unsteady Thermoacoustic Field Inside a Rijke-Type Pulse Combustor," *Numerical Heat Transfer, Part A: Applications*, Vol. 41, No. 3, 2002, pp. 245–262. doi:10.1080/10407780252780153.
- [8] Feldman, K. T., "Review of the Literature on Rijke Thermoacoustic Phenomena," *Journal of Sound and Vibration*, Vol. 7, 1968, pp. 83–89. doi:10.1016/0022-460X(68)90159-4.
- [9] Feldman, K. T., "Review of the Literature on Soundhauss Thermoacoustic Phenomena," *Journal of Sound and Vibration*, Vol. 7, 1968, pp. 71–82. doi:10.1016/0022-460X(68)90158-2.
- [10] Bai, T., Cheng, X. C., Daniel, B. R., Jagoda, J. I., and Zinn, B. T., "Performance of a Gas Burning Rijke Pulse Combustor with Tangential Reactants Injection," *Combustion Science and Technology*, Vol. 94, No. 1-6, 1993, pp. 1– 10. doi:10.1080/00102209308935300.
- [11] Wall, T. F., Bhattacharya, S. P., Baxter, L. L., Richards, G., and Harb, J. N., "Character of Ash Deposits and the Thermal Performance of Furnaces," *Fuel Processing Technology*, Vol. 44, No. 1-3, 1995, pp. 143–153. doi:10.1016/0378-3820(94)00112-7.
- [12] Reiner, D., Xu, Z. X., Su, A., Bai, T., Daniel, B. R., and Zinn, B. T., "Combustion of Heavy Liquid Fuels in a Rijke Type Pulse Combustor," *Combustion Instabilities Driven by Thermo-Chemical Acoustic Sources*, Vol. NCA 4, 1989, pp. 1–9.
- [13] Meng, X., de Jong, W., and Kudra, T., "A state-of-the-art review of pulse combustion: Principles, modeling, applications and R&D issues," Vol. 55, mar 2016, pp. 73–114. doi:10.1016/j.rser.2015.10.110.
- [14] Yavuzkurt, S., Ha, M. Y., Koopmann, G., and Scaroni, A. W., "Model of the Enhancement of Coal Combustion using High-Intensity Acoustic Fields," *Journal of Energy Resources Technology-Transactions of the ASME*, Vol. 113, No. 4, 1991, pp. 277–285. doi:10.1115/1.2905912.
- [15] Stewart, C. R., Lemieux, P. M., and Zinn, B. T., "Application of Pulse Combustion to Solid and Hazardous Waste Incineration," Combustion Science and Technology, Vol. 94, No. 1-6, 1993, pp. 427–446. doi:10.1080/00102209308935322.
- [16] Richards, George A., W. M. J. M. G. J., "Pulse Combustor with Controllable Oscillations," June 1992.
- [17] Hoffman, T. L. and Koopmann, G. H., "Visualization of Acoustic Particle Interaction and Agglomeration: Theory Evaluation," *Journal of the Acoustical Society of America*, Vol. 101, No. 6, 1997, pp. 3421–3429. doi:10.1121/1.418352.
- [18] Hoffmann, T. L., Chen, W., Koopmann, G. H., Scaroni, A. W., and Song, L., "Experimental and Numerical Analysis of Bimodal Acoustic Agglomeration," Vol. 115, No. 3, July 1993, pp. 232–240. doi:10.1115/1.2930338.
- [19] Hoffmann, T. L. and Koopmann, G. H., "New Technique for Visualization of Acoustic Particle Agglomeration," *Review of Scientific Instruments*, Vol. 65, No. 5, 1994, pp. 1527–1536. doi:10.1063/1.1144887.
- [20] Miller, N., Powell, E. A., Chen, F., and Zinn, B. T., "Use of Air Staging to Reduce the NOx Emissions from Coal Burning Rijke Pulse Combustors," *Combustion Science and Technology*, Vol. 94, No. 1-6, 1993, pp. 411–426. doi:10.1080/00102209308935321.

- [21] Reethof, G., "Acoustic Agglomeration of Power Plant Fly Ash for Environmental and Hot Gas Clean-up," *Journal of Vibration and Acoustics-Transactions of the ASME*, Vol. 110, No. 4, 1988, pp. 552–557. doi:10.1115/1.3269565.
- [22] Reethof, G., Song, L., and Koopmann, G., "Experimental and theoretical results of acoustic agglomeration at high pressures and high temperatures," Vol. 87, No. S1, May 1990, pp. S21–S22. doi:10.1121/1.2028126.
- [23] Sharifi, R., Miller, S. F., Scaroni, A. W., Koopmann, G. H., and Chen, W., "In Situ Monitoring of the Acoustic Agglomeration of Fly Ash Particles," ASME, International Gas Turbine Institute, Vol. 9, 1994, pp. 549–555.
- [24] Song, L., Koopmann, G. H., and Hoffmann, T. L., "An Improved Theoretical Model of Acoustic Agglomeration," *Journal of Vibration and Acoustics-Transactions of the ASME*, Vol. 116, No. 2, 1994, pp. 208–214. doi:10.1115/1.2930414.
- [25] Tiwary, R. and Reethof, G., "Effect of Hydrodynamic Interaction between Small Particles on Fillup of Agglomeration Volume in Acoustic Agglomeration of Aerosols," ASME Winter Annual Meeting, Vol. 87-WA/NCA-4, 1987, pp. 1–7.
- [26] Tiwary, R. and Reethof, G., "Numerical Simulation of Acoustic Agglomeration and Experimental Verification," *Journal of Vibration and Acoustics-Transactions of the ASME*, Vol. 109, No. 2, 1987, pp. 185–191. doi:10.1115/1.3269412.
- [27] Bai, T., Cheng, X. C., Daniel, B. R., Jagoda, J. I., and Zinn, B. T., "Vortex Shedding and Periodic Combustion Processes in a Rijke Type Pulse Combustor," *Combustion Science and Technology*, Vol. 94, No. 1-6, 1993, pp. 245–258. doi:10.1080/00102209308935313.
- [28] Carvalho, J. A., Miller, N., Daniel, B. R., and Zinn, B. T., "Combustion Characteristics of Unpulverized Coal Under Pulsating and Non-Pulsating Conditions," *Fuel*, Vol. 66, No. 1, 1987, pp. 4–8. doi:10.1016/0016-2361(87)90202-X.
- [29] George, W. and Reethof, G., "On the Fragility of Acoustically Agglomerated Submicron Fly Ash Particles," *Journal of Vibration, Acoustics, Stress, and Reliability in Design*, Vol. 108, 1986, pp. 332–329. doi:10.1115/1.3269346.
- [30] Chen, T. Y., Hegde, U. G., Daniel, B. R., and Zinn, B. T., "Flame Radiation and Acoustic Intensity Measurements in Acoustically Excited Diffusion Flames," *Journal of Propulsion and Power*, Vol. 9, No. 2, 1993, pp. 210–216. doi:10.2514/3.23611.
- [31] Carvalho, J., Wang, M., Miller, N., Daniel, B., and Zinn, B., "Controlling mechanisms and performance of coal burning rijke type pulsating combustors," Vol. 20, No. 1, January 1985, pp. 2011–2017. doi:10.1016/s0082-0784(85)80701-3.
- [32] Zinn, B. T., "Pulse Combustion: Recent Applications and Research Issues," Proceedings of the 24th International Symposium on Combustion, Vol. 19626, Combustion Institute, 1992, pp. 1297–1305. doi:10.1016/S0082-0784(06)80151-7.
- [33] Reuter, D., Daniel, B. R., Jagoda, J., and Zinn, B. T., "Periodic Mixing and Combustion Processes in Gas Fired Pulsating Combustors," *Combustion and Flame*, Vol. 65, No. 3, 1986, pp. 281–290. doi:10.1016/0010-2180(86)90042-8.
- [34] Xu, Z. X., Reiner, D., Su, A., Bai, T., Daniel, B. R., and Zinn, B. T., "Flame Stabilization and Combustion of Heavy Liquid Fuels in a Rijke Type Pulse Combustor," *Fossil Fuel Combustion*, Vol. PD 33, ASME, Petroleum Division, 1991, pp. 17–26.
- [35] Richards, G. A., Logan, R. G., Meyer, C. T., and Anderson, R. J., "Ash Deposition at Coal-Fired Gas Turbine Conditions: Surface and Combustion Temperature Effects," *Journal of Engineering for Gas Turbines and Power-Transactions of the ASME*, Vol. 114, No. 1, 1992, pp. 132–138. doi:10.1115/1.2906295.
- [36] Richards, G. A., Morris, G. J., Shaw, D. W., Keeley, S. A., and Welter, M. J., "Thermal Pulse Combustion," *Combustion Science and Technology*, Vol. 94, No. 16, 1993, pp. 57–85. doi:10.1080/00102209308935304.
- [37] Yavuzkurt, S., Ha, M. Y., Reethof, G., Koopmann, G., and Scaroni, A. W., "Effect of an Acoustic Field on the Combustion of Coal Particles in a Flat Flame Burner," *Journal of Energy Resources Technology-Transactions of the ASME*, Vol. 113, No. 4, 1991, pp. 286–293. doi:10.1115/1.2905913.
- [38] Lieuwen, T. and Zinn, B., "The Role of Equivalence Ratio Oscillations in Driving Combustion Instabilities in Low NOx Gas Turbines," *Proceedings of the 27th International Symposium on Combustion*, Vol. 27, No. 2, 1998, pp. 1809–1816. doi:10.1016/S0082-0784(98)80022-2.
- [39] Tiwary, R. and Reethof, G., "Hydrodynamic Interaction of Spherical Aerosol Particles in a High Intensity Acoustic Field," *Journal of Sound and Vibration*, Vol. 108, 1986, pp. 33–49. doi:10.1016/S0022-460X(86)80309-1.
- [40] Hedge, U. G. and Zinn, B. T., "Theoretical Investigation of Reactive Acoustic Boundary Layers in Porous Walled Ducts," Chemical and Physical Processes in Combustion, Vol. 60, No. 4, 1984, pp. 1–60.

- [41] Fabignon, Y., Dupays, J., Avalon, G., Vuillot, F., Lupoglazoff, N., Casalis, G., and Prévost, M., "Instabilities and pressure oscillations in solid rocket motors," *Journal of Aerospace Science and Technology*, Vol. 7, No. 3, April 2003, pp. 191–200. doi:10.1016/S1270-9638(02)01194-X.
- [42] Price, E. W., "Review of Combustion Instability Characteristics of Solid Propellants," *AGARD Conference Proceedings*, Vol. 1 of *Advances in Tactical Rocket Propulsion*, Technivision Services, 1968, pp. 141–194.
- [43] Majdalani, J., Flandro, G. A., and Fischbach, S. R., "Some Rotational Corrections to the Acoustic Energy Equation in Injection-Driven Enclosures," *Physics of Fluids*, Vol. 17, No. 7, 2005, pp. 0741021–20. doi:10.1063/1.1920647.
- [44] Flandro, G. A., Fischbach, S. R., and Majdalani, J., "Nonlinear rocket motor stability prediction: Limit amplitude, triggering, and mean pressure shift," *Physics of Fluids*, Vol. 19, No. 9, 2007, pp. 094101–16. doi:10.1063/1.2746042.
- [45] Fischbach, S. and Majdalani, J., "Volume-to-Surface Reduction of Vorticoacoustic Stability Integrals," *Journal of Sound and Vibration*, Vol. 321, No. 3-5, 2009, pp. 1007–1025. doi:10.1016/j.jsv.2008.10.001.
- [46] Fischbach, S. R., Flandro, G. A., and Majdalani, J., "Acoustic Streaming in Simplified Liquid Rocket Engines with Transverse Mode Oscillations," *Physics of Fluids*, Vol. 22, No. 6, jun 2010, pp. 063602–21. doi:10.1063/1.3407663.
- [47] Nicoli, C. and Pelce, P., "One-Dimensional Model for the Rijke Tube," *Journal of Fluid Mechanics*, Vol. 202, 1989, pp. 83–96. doi:10.1017/s0022112089001102.
- [48] Hantschk, C. C. and Vortmeyer, D., "Numerical Simulation of Self-Excited Thermoacoustic Instabilities in a Rijke Tube," *Journal of Sound and Vibration*, Vol. 227, No. 3, 1999, pp. 511–522. doi:10.1006/jsvi.1999.2296.
- [49] Matveev, K. I. and Culick, F. E. C., "A model for combustion instability involving vortex shedding," Combustion Science and Technology, Vol. 175, No. 6, jun 2003, pp. 1059–1083. doi:10.1080/00102200302349.
- [50] Matveev, K. I. and Culick, F. E. C., "A Study of the Transition to Instability in a Rijke Tube with Axial Temperature Gradient," *Journal of Sound and Vibration*, Vol. 264, No. 3, 2003, pp. 689–706. doi:10.1016/s0022-460x(02)01217-8.
- [51] Matveev, K. I., *Thermoacoustic Instabilities in the Rijke Tube: Experiments and Modeling*, Thesis, California Institute of Technology, 2003.
- [52] Bigongiari, A. and Heckl, M., "A Green's Function Approach to the Study of Hysteresis in a Rijke Tube," *Proceedings of the 22nd International Congress of Sound and Vibration*, Florence, Italy, 2015.
- [53] Bigongiari, A. and Heckl, M. A., "A Green's Function Approach to the Rapid Prediction of Thermoacoustic Instabilities in Combustors," *Journal of Fluid Mechanics*, Vol. 798, 2016, pp. 970–996. doi:10.1017/jfm.2016.332.
- [54] Heckl, M. A. and Howe, M. S., "Stability Analysis of the Rijke Tube with a Green's Function Approach," *Journal of Sound and Vibration*, Vol. 305, No. 4-5, 2007, pp. 672–688. doi:10.1016/j.jsv.2007.04.027.
- [55] Heckl, M. A., "The Rijke Tube: A Green's Function Approach in the Frequency Domain," Acta Acustica United with Acustica, Vol. 96, No. 4, 2010, pp. 743–752. doi:10.3813/aaa.918328.
- [56] Juniper, M. P., "Triggering in the Horizontal Rijke Tube: Non-Normality, Transient Growth and Bypass Transition," *Journal of Fluid Mechanics*, Vol. 667, 2011, pp. 272–308. doi:10.1017/s0022112010004453.
- [57] Magri, L. and Juniper, M. P., "Sensitivity Analysis of a Time-Delayed Thermo-Acoustic System via an Adjoint-Based Approach," *Journal of Fluid Mechanics*, Vol. 719, 2013, pp. 183–202. doi:10.1017/jfm.2012.639.
- [58] Juniper, M. P. and Sujith, R. I., "Sensitivity and Nonlinearity of Thermoacoustic Oscillations," Vol. 50, 2018, pp. 661–689. doi:10.1146/annurev-fluid-122316-045125.
- [59] Balasubramanian, K. and Sujith, R. I., "Thermoacoustic Instability in a Rijke Tube: Non-Normality and Nonlinearity," *Physics of Fluids*, Vol. 20, No. 4, 2008, pp. 044103–11. doi:10.1063/1.2895634.
- [60] Zhao, D. and Chow, Z. H., "Thermoacoustic Instability of a Laminar Premixed Flame in Rijke Tube with a Hydrodynamic Region," *Journal of Sound and Vibration*, Vol. 332, No. 14, 2013, pp. 3419–3437. doi:10.1016/j.jsv.2013.01.031.
- [61] Reynst, F. H., Pulsating Combustion The Collected Works of F. H. Reynst, Pergamom Press, New York, 1961.
- [62] Zinn, B. T., Miller, N., Carvalho, J. A., and Daniel, B. R., "Pulsating Combustion of Coal in a Rijke Type Combustor," Proceedings of the 19th International Symposium on Combustion, Vol. 19, 1982, pp. 1197–1203.

- [63] McIntosh, A., "Pressure Disturbances of Different Length Scales Interacting with Conventional Flames," Combustion Science and Technology, Vol. 75, No. 4-6, 1991, pp. 287–309. doi:10.1080/00102209108924093.
- [64] Majdalani, J., Entezam, B., and Van Moorhem, W. K., "The Rijke Tube Revisited Via Laboratory and Numerical Experiments," 35th AIAA Thermophysics Conference, AIAA Paper 2001-2961, Anaheim, CA, June 2001. doi:10.2514/6.2001-2961.
- [65] Yoon, M., "The Entropy Wave Generation in a Heated One-Dimensional Duct," *Journal of Fluid Mechanics*, Vol. 883, 2020, pp. A44–24. doi:10.1017/jfm.2019.901.
- [66] Sugimoto, N. and Yoshida, M., "Marginal Condition for the Onset of Thermoacoustic Oscillations of a Gas in a Tube," *Physics of Fluids*, Vol. 19, No. 7, 2007, pp. 074101–13. doi:10.1063/1.2742422.
- [67] Sugimoto, N., Shimizu, D., and Kimura, Y., "Evaluation of Mean Energy Fluxes in Thermoacoustic Oscillations of a Gas in a Tube," *Physics of Fluids*, Vol. 20, No. 2, 2008, pp. 024103–13. doi:10.1063/1.2837176.
- [68] Biwa, T., Sobata, K., Otake, S., and Yazaki, T., "Observation of thermoacoustic shock waves in a resonance tube," *The Journal of the Acoustical Society of America*, Vol. 136, No. 3, sep 2014, pp. 965–968. doi:10.1121/1.4892782.
- [69] White, F. M. and Majdalani, J., Viscous Fluid Flow, McGraw-Hill, 2021.
- [70] Farouk, B., Oran, E. S., and Fusegi, T., "Numerical Study of Thermoacoustic Waves in an Enclosure," *Physics of Fluids*, Vol. 12, No. 5, 2000/05/01 2000, pp. 1052–1061. doi:10.1063/1.870360.
- [71] Hirt, C. W. and Nichols, B. D., "Volume of Fluid (VOF) Method for the Dynamics of Free Boundaries," *Journal of Computational Physics*, Vol. 39, 1981, pp. 201–225. doi:10.1016/0021-9991(81)90145-5.
- [72] Flow-3D, "Flow Science Incorporated," 2001.
- [73] Carvalho, J. A., Ferreira, C., Bressan, C., and Ferreira, G., "Definition of Heater Location to Drive Maximum Amplitude Acoustic Oscillations in a Rijke Tube," *Combustion and Flame*, Vol. 76, No. 1, 1989, pp. 17–27. doi:10.1016/0010-2180(89)90073-4.
- [74] Entezam, B., Van Moorhem, W. K., and Majdalani, J., "Modeling of a Rijke-Tube Pulse Combustor using Computational Fluid Dynamics," 33rd AIAA/ASME/SAE/ASEE Joint Propulsion Conference, AIAA Paper 97-2718, 1997. doi:10.2514/6.1997-2718.
- [75] Rijke, P. L., "LXXI. Notice of a New Method of Causing a Vibration of the Air Contained in a Tube Open at Both Ends," The London, Edinburgh, and Dublin Philosophical Magazine and Journal of Science, Vol. 17, No. 116, 1859, pp. 419–422. doi:10.1080/14786445908642701.
- [76] Noiray, N., Durox, D., Schuller, T., and Candel, S., "A Unified Framework for Nonlinear Combustion Instability Analysis Based on the Flame Describing Function," *Journal of Fluid Mechanics*, Vol. 615, nov 2008, pp. 139. doi:10.1017/s0022112008003613.
- [77] Noble, A. C., King, G. B., Laurendeau, N. M., Gord, J. R., and Roy, S., "Nonlinear Thermoacoustic Instability Dynamics in a Rijke Tube," *Combustion Science and Technology*, Vol. 184, No. 3, March 2012, pp. 293–322. doi:10.1080/00102202.2011.635614.
- [78] Sujith, R. I., Juniper, M. P., and Schmid, P. J., "Non-Normality and Nonlinearity in Thermoacoustic Instabilities," *International Journal of Spray and Combustion Dynamics*, Vol. 8, No. 2, jun 2016, pp. 119–146. doi:10.1177/1756827716651571.
- [79] Sujith, R. I., Waldherr, G. A., and Zinn, B. T., "An Exact Solution for One-Dimensional Acoustic Fields in Ducts with an Axial Temperature-Gradient," *Journal of Sound and Vibration*, Vol. 184, No. 3, 1995, pp. 389–402. doi:10.1006/jsvi.1995.0323.
- [80] Sujith, R. I., "Exact Solutions for Modeling Sound Propagation Through a Combustion Zone," *Journal of the Acoustical Society of America*, Vol. 110, No. 4, 2001, pp. 1839–1844. doi:10.1121/1.1396332.
- [81] Bednarik, M., Cervenka, M., Lotton, P., and Penelet, G., "Behavior of Plane Waves Propagating through a Temperature-Inhomogeneous Region," *Journal of Sound and Vibration*, Vol. 362, 2016, pp. 292–304. doi:10.1016/j.jsv.2015.10.010.
- [82] Kumar, B. M. and Sujith, R. I., "Exact Solution for One-Dimensional Acoustic Fields in Ducts with a Quadratic Mean Temperature Profile," *Journal of the Acoustical Society of America*, Vol. 101, No. 6, 1997, pp. 3798–3799. doi:10.1121/1.418385.

- [83] Kumar, B. M. and Sujith, R. I., "Exact Solution for One-Dimensional Acoustic Fields in Ducts with Polynomial Mean Temperature Profiles," *Journal of Vibration and Acoustics-Transactions of the ASME*, Vol. 120, No. 4, 1998, pp. 965–969. doi:10.1115/1.2893927.
- [84] Munjal, M. L. and Prasad, M. G., "On Plane-Wave Propagation in a Uniform Pipe in the Presence of a Mean Flow and a Temperature Gradient," *The Journal of the Acoustical Society of America*, Vol. 80, No. 5, 1986, pp. 1501–1506. doi:10.1121/1.394406.
- [85] Cummings, A., "Ducts with Axial Temperature Gradients: An Approximate Solution for Sound Transmission and Generation," *Journal of Sound and Vibration*, Vol. 51, No. 1, 1977, pp. 55–67. doi:10.1016/S0022-460X(77)80112-0.
- [86] Li, J. and Morgans, A. S., "The One-Dimensional Acoustic Field in a Duct with Arbitrary Mean Axial Temperature Gradient and Mean Flow," *Journal of Sound and Vibration*, Vol. 400, 2017, pp. 248–269. doi:10.1016/j.jsv.2017.03.047.
- [87] Kovasznay, L. S. G., "Turbulence in Supersonic Flow," *Journal of the Aeronautical Sciences*, Vol. 20, No. 10, oct 1953, pp. 657–674. doi:10.2514/8.2793.
- [88] Dowling, A. P., "The Calculation of Thermoacoustic Oscillations," *Journal of Sound and Vibration*, Vol. 180, No. 4, 1995, pp. 557–581. doi:10.1006/jsvi.1995.0100.
- [89] Philip M. Morse, K. U. I., Theoretical Acoustics, Princeton University Press, Jan. 1987.
- [90] Polyanin, A. D., Handbook of Linear Partial Differential Equations for Engineers and Scientists, Chapman and Hall/ CRC, 2002.
- [91] Kosztin, B., Heckl, M., Muller, R., and Hermann, J., "Thermo-Acoustic Properties of a Burner with Axial Temperature Gradient: Theory and Experiment," *International Journal of Spray and Combustion Dynamics*, Vol. 5, No. 1, 2013, pp. 67–84. doi:10.1260/1756-8315.5.1.67.
- [92] Lieuwen, T. C., Unsteady Combustor Physics, Cambridge University Press, 2012.
- [93] Ledoux, V. and Van Daele, M., "Matslise 2.0: A Matlab Toolbox for Sturm–Liouville Computations," *ACM Transactions on Mathematical Software*, Vol. 42, No. 4, 2016, pp. 1–18. doi:10.1145/2839299.